Energizing Star Formation: The Cosmic-Ray Ionization Rate in NGC 253 Derived from ALCHEMI Measurements of H₃O⁺ and SO

Jonathan Holdship[1,2], Jeffrey G. Mangum[3], Serena Viti[1,2], Erica Behrens[4], Nanase Harada[5,6], Sergio Martín[7,8],
Kazushi Sakamoto[9], Sebastien Muller[10], Kunihiko Tanaka[11], Kouichiro Nakanishi[6,12], Rubén Herrero-Illana[7,13],
Yuki Yoshimura[14], Rebeca Aladro[15], Laura Colzi[16,17], Kimberly L. Emig[3], Christian Henkel[15,18],
Yuri Nishimura[19,20], Víctor M. Rivilla[16,17], and Paul P. van der Werf[21]
(ALMA Comprehensive High-resolution Extragalactic Molecular Inventory (ALCHEMI) collaboration)

[1] Leiden Observatory, Leiden University, PO Box 9513, NL-2300 RA Leiden, The Netherlands; holdship@strw.leidenuniv.nl
[2] Department of Physics and Astronomy, University College London, Gower Street, London WC1E 6BT, UK
[3] National Radio Astronomy Observatory, 520 Edgemont Road, Charlottesville, VA 22903-2475, USA
[4] Department of Astronomy, University of Virginia, P.O. Box 400325, 530 McCormick Road, Charlottesville, VA 22904-4325, USA
[5] National Astronomical Observatory of Japan, 2-21-1 Osawa, Mitaka, Tokyo 181-8588, Japan
[6] Department of Astronomy, School of Science, The Graduate University for Advanced Studies (SOKENDAI), 2-21-1 Osawa, Mitaka,
Tokyo, 181-1855 Japan
[7] European Southern Observatory, Alonso de Córdova, 3107, Vitacura, Santiago 763-0355, Chile
[8] Joint ALMA Observatory, Alonso de Córdova, 3107, Vitacura, Santiago 763-0355, Chile
[9] Institute of Astronomy and Astrophysics, Academia Sinica, 11F of AS/NTU Astronomy-Mathematics Building, No. 1, Sec. 4, Roosevelt Road, Taipei 10617, Taiwan
[10] Department of Space, Earth and Environment, Chalmers University of Technology, Onsala Space Observatory, SE-43992 Onsala, Sweden
[11] Department of Physics, Faculty of Science and Technology, Keio University, 3-14-1 Hiyoshi, Yokohama, Kanagawa 223–8522 Japan
[12] National Astronomical Observatory of Japan, 2-21-1 Osawa, Mitaka, Tokyo 181-8588, Japan
[13] Institute of Space Sciences (ICE, CSIC), Campus UAB, Carrer de Magrans, E-08193 Barcelona, Spain
[14] Institute of Astronomy, Graduate School of Science, The University of Tokyo, 2-21-1 Osawa, Mitaka, Tokyo 181-0015, Japan
[15] Max-Planck-Institut für Radioastronomie, Auf dem Hügel 69, D-53121 Bonn, Germany
[16] Centro de Astrobiología (CSIC-INTA), Ctra. de Ajalvir Km. 4, 28850, Torrejón de Ardoz, Madrid, Spain
[17] INAF-Osservatorio Astrofisico di Arcetri, Largo E. Fermi 5, I-50125, Florence, 5 Italy
[18] Astronomy Department, Faculty of Science, King Abdulaziz University, P.O. Box 80203, Jeddah 21589, Saudi Arabia
[19] Institute of Astronomy, The University of Tokyo, 2-21-1, Osawa, Mitaka, Tokyo 181-0015, Japan
[20] ALMA Project, National Astronomical Observatory of Japan, 2-21-1, Osawa, Mitaka, Tokyo 181-8588, Japan
[21] Leiden Observatory, Leiden University, PO Box 9513, NL - 2300 RA Leiden, The Netherlands

Abstract

The cosmic-ray ionization rate (CRIR) is a key parameter in understanding the physical and chemical processes in the interstellar medium. Cosmic rays are a significant source of energy in star formation regions, impacting the physical and chemical processes that drive the formation of stars. Previous studies of the circum-molecular zone of the starburst galaxy NGC 253 have found evidence for a high CRIR value: 10^3–10^6 times the average CRIR within the Milky Way. This is a broad constraint, and one goal of this study is to determine this value with much higher precision. We exploit ALMA observations toward the central molecular zone of NGC 253 to measure the CRIR. We first demonstrate that the abundance ratio of H₃O⁺ and SO is strongly sensitive to the CRIR. We then combine chemical and radiative transfer models with nested sampling to infer the gas properties and CRIR of several star-forming regions in NGC 253 from emission from their transitions. We find that each of the four regions modeled has a CRIR in the range $(1$–$80) \times 10^{-14}$ s^{-1} and that this result adequately fits the abundances of other species that are believed to be sensitive to cosmic rays, including C₂H, HCO⁺, HOC⁺, and CO. From shock and photon-dominated/X-ray dominated region models, we further find that neither UV-/X-ray-driven nor shock-dominated chemistry is a viable single alternative as none of these processes can adequately fit the abundances of all of these species.

Unified Astronomy Thesaurus concepts: Starburst galaxies (1570); Interstellar medium (847); Active galaxies (17); Interstellar abundances (832)

Supporting material: machine-readable table

1. Introduction

Cosmic rays play an important role in the interstellar medium as a source of heating and ionization. They drive chemistry by ionizing atoms; many gas-phase reaction chains begin with ionization followed by a barrierless reaction (Williams & Viti 2013). Moreover, interactions with cosmic rays heat the gas (Goldsmith 2001), which can spur more complex chemistry and also affect the dynamics of the system in question.

It is clear that measuring the cosmic-ray ionization rate (CRIR) is vital to understanding the chemical and dynamical evolution of molecular clouds. Careful measurement of the CRIR is required in order to properly characterize the energy budget within star formation regions. For this reason, there have been many efforts to measure the CRIR in the Milky Way (e.g., Padovani et al. 2009; Indriolo et al. 2015) and in extragalactic environments (e.g., González-Alfonso et al. 2013;

Muller et al. 2016). These measurements typically use ratios of OH^+, H_2O^+, and H_3O^+ to infer the CRIR assuming chemical equilibrium has been reached.

In this work, we attempt to infer the average CRIR for several regions in the central molecular zone (CMZ) of the starburst galaxy NGC 253 using other molecular line ratios. Due to its rich molecular emission, NGC 253 was selected as the target of the ALMA Comprehensive High-Resolution Extragalactic Molecular Inventory (ALCHEMI), an ALMA large program (Martín et al. 2021). The goal of ALCHEMI is to produce the most complete molecular inventory of an extragalactic object and use that to drive understanding of the CMZ.

The CMZ of NGC 253 contains several large ($\sim$50 pc), dense ($\sim 1 \times 10^5$ cm^{-3}), well-studied molecular clouds (e.g., Sakamoto et al. 2011; Leroy et al. 2018), which are labeled in Figure 1. Often labeled as giant molecular clouds (GMCs) due to their size, they have much higher masses and have higher velocity dispersions (Leroy et al. 2015) than typical GMCs in the Milky Way. We refer to these GMC-like structures as GMCs for simplicity throughout this work. See Leroy et al. (2015) for position information associated with these GMCs and Mangum et al. (2019) for the association of these GMCs with other identified dense gas positions in NGC 253. It is for the brightest of these GMCs (3, 4, 5, 6, and 7), closest to the center of the CMZ, that we intend to infer the CRIR.

Previous work has attempted to measure the CRIR in the GMCs of NGC 253. For example, Holdship et al. (2021) found that a high C_2H abundance in the GMCs was likely caused by cosmic rays. However, an attempt to use chemical modeling to measure the CRIR found that it could only be constrained in the range 1×10^{-14}–1×10^{-11} s^{-1} due to the low sensitivity of the C_2H abundance to the CRIR. Meanwhile, Harada et al. (2021) found that HCO^+ and HOC^+ measurements indicated a CRIR $>1 \times 10^{-14}$ s^{-1} confirming—but not further constraining—the previous measurement. Despite these large uncertainties, it is clear the CRIR in these regions is much higher than the Galactic value, which is typically measured to be in the range of 1×10^{-17}–10×10^{-17} s^{-1} (Padovani et al. 2009; Indriolo et al. 2015). More sensitive tracers are required to obtain robust and accurate measurements of the CRIR in star-forming regions. In this work, we consider H_3O^+ and SO because their abundance ratio has previously been found to be strongly dependent on the CRIR (Bayet et al. 2011). We first confirm this dependency using a large grid of chemical models and then use emission from these species to infer the CRIR in the CMZ of NGC 253.

In Section 2, the data reduction steps followed to extract line intensities from the ALCHEMI image cubes are described. In Section 3 we present preliminary modeling to justify our analysis and the approach used to infer the CRIR for the targeted GMCs of NGC 253. In Section 4 we present the results of the analysis, which is discussed in Section 5. We present our summary in Section 6.

2. Observational Data

2.1. ALCHEMI Data

We make use of data acquired as part of the ALCHEMI ALMA large program. A full description of the ALCHEMI observations and data reduction can be found in Martín et al. (2021) but important details are given here. ALCHEMI is an unbiased spectral survey of the central molecular zone (CMZ) of

the starburst galaxy NGC 253 covering ALMA bands 3 through 7 (84–373 GHz).

NGC 253 was observed toward a nominal phase center of $\alpha = 00^h47^m33^s26$, $\delta = -25°17'17''7$ (ICRS). Observations were configured to cover a common rectangular area of $50'' \times 20''$ with a position angle of $65°$ (east of north). All ALCHEMI image cubes presented in this article were imaged to a common beam size of $1''6$. The maximum recoverable scale for the ALCHEMI observations is $15''$. If the distance of NGC 253 is taken to be 3.5 Mpc (Rekola et al. 2005), these angular size scales correspond to linear size scales of 28 and 250 pc, respectively. The spectral range of the ALCHEMI data includes 37 SO and 2 H_3O^+ rotational transitions. These SO and H_3O^+ transitions are listed with their frequencies and quantum numbers in Table 1. The recommended 1σ absolute flux calibration uncertainty for measurements from the ALCHEMI survey is 15% (Martín et al. 2021), a value that we adopt in the analysis presented in this article. We have also extracted the continuum emission associated with the ALCHEMI measurements listed in Table 1 using the continuum subtraction and imaging process described in Martín et al. (2021).

2.2. Additional ALMA Archival Data

Only two transitions of H_3O^+ are contained in the ALCHEMI data. This may limit our ability to constrain our fits, and therefore, we augmented the ALCHEMI data analyzed with ALMA archival measurements of the H_3O^+ 3_0–2_0 transition. This transition has a rest frequency of 396.272 GHz, and the data were taken from ALMA project 2016.1.01285.S (PI: Jesus Martín-Pintado). These data include imaging of a single primary beam (PB) toward phase center position $\alpha = 00^h47^m33^s134$, $\delta = -25°17'19''68$ (ICRS) with the ACA ($\theta_{PB} = 38''$) and 12 m array ($\theta_{PB} = 22''$). The observed phase center position for these measurements is within $2''$ of the observed phase center for the ALCHEMI measurements (Section 2.1). In order to directly compare these H_3O^+ 3_0–2_0 measurements with our other H_3O^+ and SO measurements extracted from the ALCHEMI archive, we have imaged the H_3O^+ 3_0–2_0 observations using the ALCHEMI imaging pipeline (Martín et al. 2021). Starting with the ALMA-calibrated measurement set from the ALMA archive, we produced continuum-subtracted H_3O^+ 3_0–2_0 image cubes using a robust parameter of 0.5. To match the spatial and spectral resolution of the ALCHEMI measurements, the H_3O^+ 3_0–2_0 images were imaged to a spatial and spectral resolution of $1.6''$ and 10 km s^{-1}, respectively. The final spectral channel rms of these images is 2.6 mJy beam^{-1}. The ALMA recommendation for the 1σ absolute flux calibration uncertainty for measurements from ALMA Band 8 is 20% (ALMA Cycle 4 Proposer's Guide, Section A.9.2), a value that we adopt for the subsequent analysis of these H_3O^+ 3_0–2_0 measurements. We have also extracted the continuum emission associated with these measurements using the continuum subtraction and imaging process described in Martín et al. (2021).

2.3. Spectral Line Overlap

Local thermodynamic equilibrium (LTE) modeling of the ALCHEMI data (Martín et al. 2021) showed that the moderate line widths ($\Delta v \simeq 75$ km s^{-1} FWHM) of the transitions detected toward NGC 253 cause many transitions to overlap. As a result, measuring the emission above the noise in the vicinity of each of our transitions will often result in total integrated intensities that include flux from other transitions.
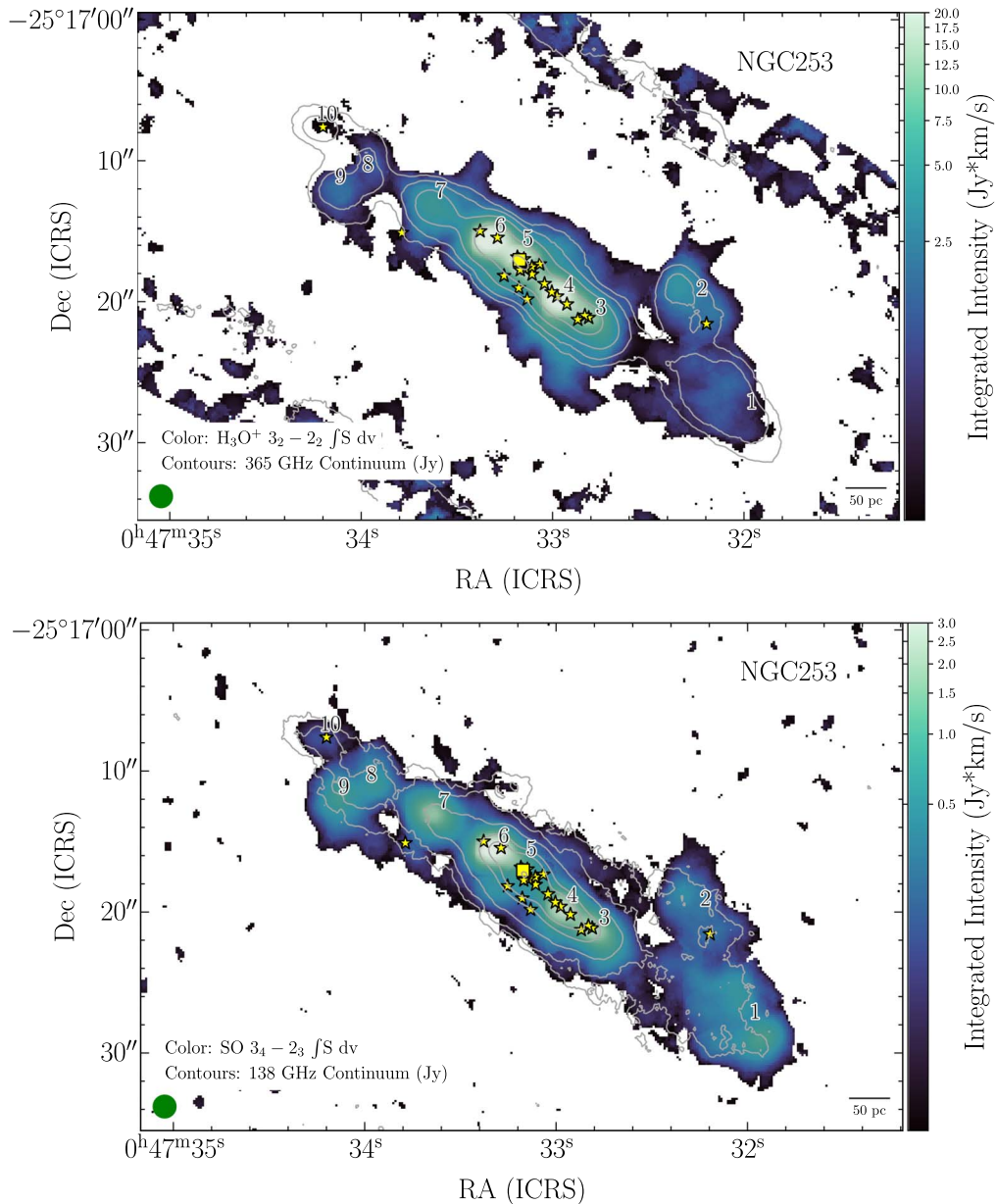
Figure 1. Sample H_3O^+ (top) and SO (bottom) integrated intensity (moment 0) images toward NGC 253. For each image, the green ellipse and black scale bar in the lower-left and lower-right corners show the final imaged beam size (1.6 arcsec) and physical scale, respectively. Red numbers indicate the locations of the dense molecular emission regions identified by Leroy et al. (2015, Table 4). Star-shaped markers locate the positions of the 2 cm radio continuum emission peaks (Ulvestad et al. 1997), with a square indicating the position of the strongest radio continuum peak identified by Turner et al. (1985). The lower integrated intensity limit for each transition is set to 3σ in the integrated intensity (see Section 2.4). Overlain in contours is the associated continuum emission distribution for each transition. Continuum contours are in steps of 3, 6, 9, 12, 30, 120, 240, and 900 times the respective continuum rms, where the peak continuum intensity dictates the number of these levels actually used for a given panel. The continuum rms values for the H_3O^+ and SO transitions shown are 1.0 and 0.15 mJy beam^{-1}, respectively.

In order to estimate which of our SO and H_3O^+ transitions are expected to be significantly blended with an interloper, we used the modeling results described by Martín et al. (2021) as a guide, with inspection of the spectra from each GMC. Where a target SO or H_3O^+ transition was found to be potentially blended with the emission from another line, we estimate the amount of overlap between the integrated intensities of these two transitions. We then take the integrated intensity to be only the fraction of the emission that comes from the target transition.

The overlap estimate is derived by performing multiple Gaussian fits to spectra drawn through beam-sized areas centered on the position of each GMC. The interloper overlap correction using these sample spectra is defined as

$$\text{Interloper Correction} \equiv 1 - \frac{\sum_{\text{overlap}} y_{\text{interloper}}}{\sum_{\text{overlap}} (y_{\text{target}} + y_{\text{interloper}})}, \quad (1)$$

where $y_{\text{interloper}}$ and y_{target} are the intensities of the relative frequency-constrained Gaussian fits to the target and interloper transitions, respectively, within a spectral channel. The sum $\sum_{\text{overlap}}$ is taken over all spectral channels with a signal larger than the rms noise in the image cube under consideration. An example of the Gaussian fit analysis used to derive the interloper correction factors defined by Equation (1) and listed in Table 1 is shown in Figure 2.

Table 1
SO[a] and H_3O^+ Transitions and Frequencies

Target (1)	Frequency/GHz (2)	E_U/K (3)	Interloper (4)	Overlap Correction[b] (5)
H_3O^+ 1_1–2_1	307.192	79.5	CH_3OH 4_1–4_0	(0.25, 0.23, 0.21, 0.21, 0.24)
H_3O^+ 3_2–2_2	364.797	139.8	OCS 30–29	(1.0, 0.86, 0.88, 0.83, 1.0)
	.		HC_3N v_7 = 1 40-39	(1.0, 1.0, 0.71, 1.0, 1.0)
H_3O^+ 3_0–2_0	396.272	169.1		1.0
SO 2_2–1_1	86.093	19.3	$HC^{15}N$ 1–0	1.0
SO 2_3–1_2	99.299	9.22	NH_2CN $5_1$5–$4_1$4	1.0
SO 5_4–4_4	100.029	38.6	HC_3N 11–10	1.0
SO 3_2–2_1	109.252	21.1	HC_3N 12–11	1.0
SO 3_3–2_2	129.138	25.5		1.0
SO 6_5–5_5	136.634	50.7		1.0
SO 3_4–2_3	138.178	15.9		1.0
SO 4_3–3_2	158.971	28.7		1.0
SO 4_4–3_3	172.181	33.7	$HC^{15}N$ 2–1	1.0
SO 4_5–3_4	178.605	24.4		1.0
SO 5_4–4_3	206.176	38.6	CCS $16_1$5–$15_1$4	1.0
SO 8_7–7_7	214.357	81.2	$H_2^{34}S$ $2_2$0–$2_1$1	0.0
SO 5_5–4_4	215.220	44.1		1.0
SO 5_6–4_5	219.949	35.0		1.0
SO 2_1–1_2	236.452	15.8	HC_3N 26–25	0.0
SO 3_2–2_3	246.404	21.1	several	0.0
SO 6_5–5_4	251.825	50.7	CH_3OH $6_3$3–$6_2$4	(1.0, 0.98, 0.82, 0.97, 1.0)
	.		CH_3OH $4_3$2–$4_2$3	(0.84, 0.55, 0.87, 0.81, 0.65)
SO 9_8–8_8	254.573	99.7		1.0
SO 6_6–5_5	258.256	56.5	$HC^{15}N$ 3–2	1.0
SO 6_7–5_6	261.844	47.6	CH_3OH $2_1$1–$1_0$1	(0.88, 0.76, 0.74, 0.82, 0.89)
	.		C_2H 3_4–2_3	(1.0, 1.0, 0.91, 1.0, 1.0)
SO 4_3–3_4	267.198	28.7	HCN,v2 = 1 3–2	0.0
SO 1_1–0_1	286.340	15.2	$H_2C^{18}O$ $4_1$3–$3_1$2	1.0
SO 5_4–4_5	294.768	38.6	NH_2CHO 14_2,13–13_2,12	0.0
SO 10_9–9_9	295.356	120.2	$H_2^{34}S$ $3_3$0–$3_2$1	0.0
SO 7_6–6_5	296.550	64.9	$HCNH^+$ 4–3	(1.0, 1.0, 0.86, 1.0, 1.0)
SO 7_7–6_6	301.286	71.0		1.0
SO 7_8–6_7	304.078	61.1	SiO 7–6	1.0
			OCS 25–24	(1.0, 1.0, 0.87, 1.0, 1.0)
	.		CH_3OH $2_1$1–$2_0$2	(1.0, 1.0, 0.96, 1.0, 1.0)
SO 2_2–1_2	309.502	19.3		1.0
SO 2_1–1_0	329.385	15.8	$C^{18}O$ 3–2	0.0
SO 11_{10}–10_{10}	336.554	142.8	HC_3N 37–36	0.0
SO 3_3–2_3	339.341	25.5		1.0
SO 8_7–7_6	340.714	81.2	$HC^{18}O^+$ 4–3	(0.92, 0.87, 0.93, 0.85, 1.0)
SO 8_8–7_7	344.311	87.5	$HC^{15}N$ 4–3	(1.0, 0.99, 0.94, 0.96, 1.0)
SO 3_2–1_2	345.705	21.1	CO 3–2	0.0
SO 8_9–7_8	346.528	78.8	HC_3N,v7 = 1 38–37	(1.0, 1.0, 1.0, 0.90, 1.0)
	.		SO_2 19_1,19–18_0,18	(1.0, 1.0, 1.0, 0.98, 1.0)
SO 7_6–6_7	361.351	64.9		1.0

Notes.
[a] SO energy levels designated using the N_J notation.
[b] Overlap correction key: GMCs (3, 4, 5, 6, 7), except if all are 0.0 or 1.0.

As is apparent from the interloper correction factors listed in Table 1 and the spectrum shown in Figure 2, the overlap between the H_3O^+ 1_1–2_1 and CH_3OH 4_1–4_0 transition is quite large, as the two transitions are separated by just 26 MHz (∼2.5 spectral channels). As the H_3O^+ 1_1–2_1 transition is one of only three H_3O^+ transitions available in this study, it is important to properly assess the quality of our H_3O^+ spectral line extraction for this transition. The contribution from CH_3OH to the observed spectral profile was derived from LTE modeling using MADCUBA (Martín et al. 2019) to both the CH_3OH molecular emission across the entire ALCHEMI frequency range as well as using only nearby surrounding (in frequency

and energies) CH_3OH transitions. This LTE modeling procedure resulted in a derived H_3O^+ to CH_3OH spectral line peak intensity ratio of 0.2. Using the procedure described above, with this derived Gaussian-peak relative intensity, we derive the overlap corrections listed in Table 1.

2.4. Spectral Line Moment Extraction

Once all spectral interlopers were identified and their influence on the spectrally integrated emission from our target SO and H_3O^+ transitions assessed, we proceeded to calculate the zeroth, first, and second moments of all detected SO and
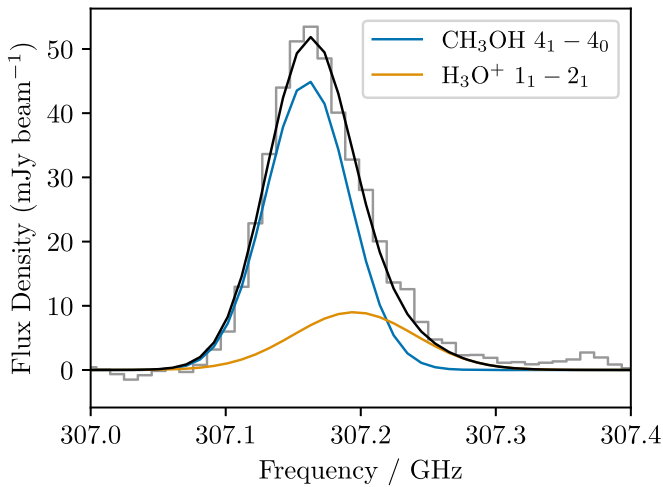
Figure 2. Observed spectrum from GMC 7 covering the H_3O^+ 1_1–2_1 transition in gray with a multiple Gaussian fit plotted in black. The color traces show the individual Gaussians used in the fit labeled by the transition, which corresponds to the central frequency. The derived interloper correction factors, using Equation (1), are listed in Table 1.

H_3O^+ transitions using the `CubeLineMoment`[22] script introduced for this same purpose by Mangum et al. (2019). `CubeLineMoment` uses a series of spectral and spatial masks to extract integrated intensities for a defined list of target spectral frequencies. As noted by Mangum et al. (2019), the `CubeLineMoment` masking process uses a bright spectral line whose velocity structure is representative of the emission over the galaxy as a "tracer" of the gas under study. In almost all of the SO and H_3O^+ transitions studied in this analysis, we use the target transition itself as the tracer transition as our target transitions are generally sufficiently intense. Final zeroth-, first-, and second-moment images were generated using a signal limit of three times that of the spectral channel baseline rms for the respective transition under study. Figure 1 shows representative samples of the H_3O^+ and SO integrated intensity (zeroth moment) images resulting from this analysis. In Appendix A we show the remaining H_3O^+ integrated intensity images and samples of SO emission from the other ALMA receiver bands from our measurements (Bands 3, 5, 6, and 7).

As a result of this extraction, we obtain the integrated line intensity of every transition in Table 1 for each GMC in the CMZ. This is done by taking the average intensity over a beam-sized region centered on the GMC centers defined by Leroy et al. (2015). We then adopt uncertainties on these intensities that combine the recommended 15% (for ALCHEMI measurements) or 20% (for H_3O^+ 3_0–2_0 measurements) absolute calibration uncertainty and the integrated noise added in quadrature. Finally, we adjust each integrated intensity by the relevant interloper correction factor given in Table 1. We do not adjust the uncertainty of a transition, choosing instead to retain the total uncertainty on the blended emission. This effectively overestimates the uncertainty on the intensity of the transition to account for our uncertainty on the interloper correction factor. All integrated intensities, uncertainties, and other relevant transition properties are uploaded in a supplementary table.

3. Modeling Approach

3.1. The Forward Model

To infer the CRIR, we require a model that can take a small number of free parameters, including the CRIR, and ultimately return line intensities for all the detected lines of H_3O^+ and SO. To do this, we combine the gas-grain chemical model UCLCHEM (Holdship et al. 2017) with RADEX (van der Tak et al. 2007) which is used via the Python package SpectralRadex.[23] We use recently published collisional rates between H_3O^+ and p-H_2 (Demes et al. 2021) as well as SO collisional data (Lique et al. 2006), both taken from the LAMDA[24] database (Schöier et al. 2005).

In the chemical models, we assume the GMCs can be modeled as uniform clouds with fixed physical conditions and a visual extinction that is sufficiently high to make photoprocesses negligible. This simple model is justified in the next section. The simplified picture allows us to use a single-point model as the only depth-dependent effect in UCLCHEM is UV attenuation, which becomes unimportant if the majority of the gas considered is at high visual extinction. This is important as even a 1D modeling approach would be computationally infeasible when combined with extensive sampling of the necessary parameter space. One caveat of this model is that it is known that the CRIR is attenuated by column density (Padovani et al. 2018). However, that attenuation is weak for the column densities considered in this work and so inferring an average value is reasonable.

The above chemical modeling requires three main inputs: the gas volume density (n_{H2}), the gas kinetic temperature (T_{kin}), and the CRIR (ζ), which will be given in units of $\zeta_0 = 1.36 \times 10^{-17}$ s^{-1} throughout this work as that is the normalization factor used in the chemical network (McElroy et al. 2013). In addition, we assume the initial elemental abundances are the depleted values from Jenkins (2009) or that they are scaled from those values by a constant metallicity factor (Z). The exception to this is sulfur, for which we treat the elemental abundance at $Z = 1$ as a free parameter (see Section 3.3). The model returns the equilibrium abundances of H_3O^+ and SO. By adding the additional parameters of the total H_2 column density (N_{H2}) of the GMC and the line width (ΔV), we can generate line intensities for all transitions of these two species by assuming a spherical GMC and utilizing RADEX. RADEX requires the column density of each species, which is obtained by multiplying the fractional abundance from the chemical model by the H_2 column density. The collisional excitation rate file for H_3O^+ only contains rates for collisions with p-H_2. For this reason, we set the p-H_2 density in RADEX to n_{H2} for H_3O^+ calculations on the grounds that assuming the o-H_2 collisional rates are equal to the p-H_2 rates must be a better approximation than assuming no collisions with o-H_2.

3.2. Model Justification

The GMCs in NGC 253 are complex, and many physical processes are at play. Thus, two things must be demonstrated to justify the use of this modeling procedure to infer the CRIR. First, we must show the forward model and, in particular, the H_3O^+ to SO ratio is sensitive to the CRIR as suggested by Bayet et al. (2011). Second, we must show that other physical
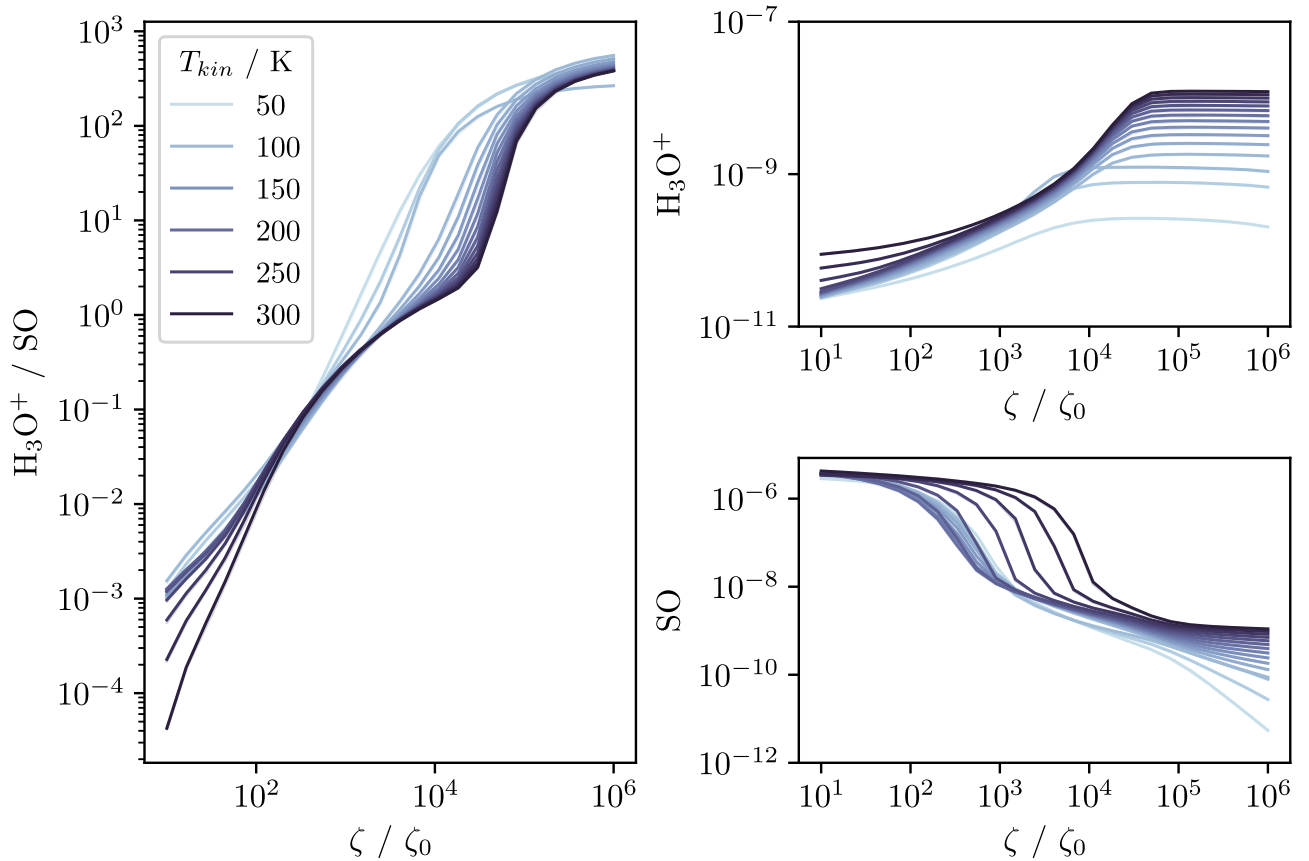
Figure 3. Equilibrium H_3O^+ and SO abundances and their ratio as a function of CRIR given in units of $\zeta_0 = 1.3 \times 10^{-17}$ s^{-1}. The abundances are averaged over models with different densities in the range of 1×10^4–1×10^7 cm^{-3}, and the color of the lines indicates the gas temperature.

or chemical processes can be ignored. At a minimum, the outer regions of any dense clouds that compose the single objects we observe at a resolution of 28 pc will be UV irradiated. Further, on larger angular scales ($\gtrsim 15''$), low-velocity shocks have been shown to be a dominant heating mechanism in the NGC 253 CMZ (Martín et al. 2006) and so shock chemistry may be at work. Thus, our simple, single-point model with negligible influence from an external UV field requires justification.

To address the model dependence on ζ, a grid of UCLCHEM models was generated in which the density, temperature, and CRIR of a cloud were varied assuming a large visual extinction. Figure 3 shows the steady-state abundances of H_3O^+ and SO across the models of this grid as well as their ratio. Both species show a clear and strong dependence on the CRIR with the H_3O^+ abundance increasing and the SO abundance decreasing in response to increasing ζ.

In the case of H_3O^+, this is driven by the fact that H_3O^+ is formed through the following chain of reactions:

$$H_2 + OH^+ \longrightarrow H_2O^+ + H$$
$$H_2 + H_2O^+ \longrightarrow H_3O^+ + H \qquad (2)$$
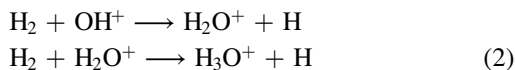
where each reaction is the primary destruction route of the ionic reactant. Therefore, the H_3O^+ abundance primarily depends on the OH^+ abundance, which is primarily produced from both reactions between O^+ and H_2 and between H^+ and OH. In both cases, the ions are formed directly by cosmic rays, and thus increasing ζ generally increases the overall H_3O^+ production rate. This ceases to be the case once ζ is such that the ionization fraction of the gas is very high. At that point, it has been shown

that increasing dissociative reactions with electrons actually drive a decrease in the H_3O^+ abundance (Gerin et al. 2010). This is most noticeable in the $T_{kin} = 50$ K case in Figure 3 where the H_3O^+ abundance actually starts to decrease at the highest ζ.

SO is a much simpler case. It forms efficiently through neutral–neutral and ion–neutral reactions in the gas phase, obtaining relatively high abundances ($\sim 1 \times 10^{-6}$) in most gas conditions. However, its primary destruction routes are reactions with ions and cosmic rays, the majority being destroyed in reactions with C^+ and H^+. Because the abundance of these reactants is directly tied to the CRIR, SO is destroyed more efficiently as ζ increases. Fortunately, this appears to be even more efficient at low temperatures, when the H_3O^+ abundance is least sensitive to ζ.

The opposite responses of these species to the CRIR result in their ratio being highly sensitive to the value of ζ. In fact, it varies by seven orders of magnitude over the explored range of ζ. Moreover, the variation in the ratio due to ζ is much larger than the variation due to temperature, so uncertainty in the gas temperature will not prevent us from inferring the CRIR. A final point to note about this preliminary modeling is that the steady-state abundances are reached quickly—typically within 1×10^5 yr. This justifies the use of equilibrium abundances for the GMCs.

To determine whether UV processes can be ignored, we use UCL_PDR[25] (Bell et al. 2006; Priestley et al. 2017) to determine whether the assumption that H_3O^+ and SO primarily arise from gas where the visual extinction is high is

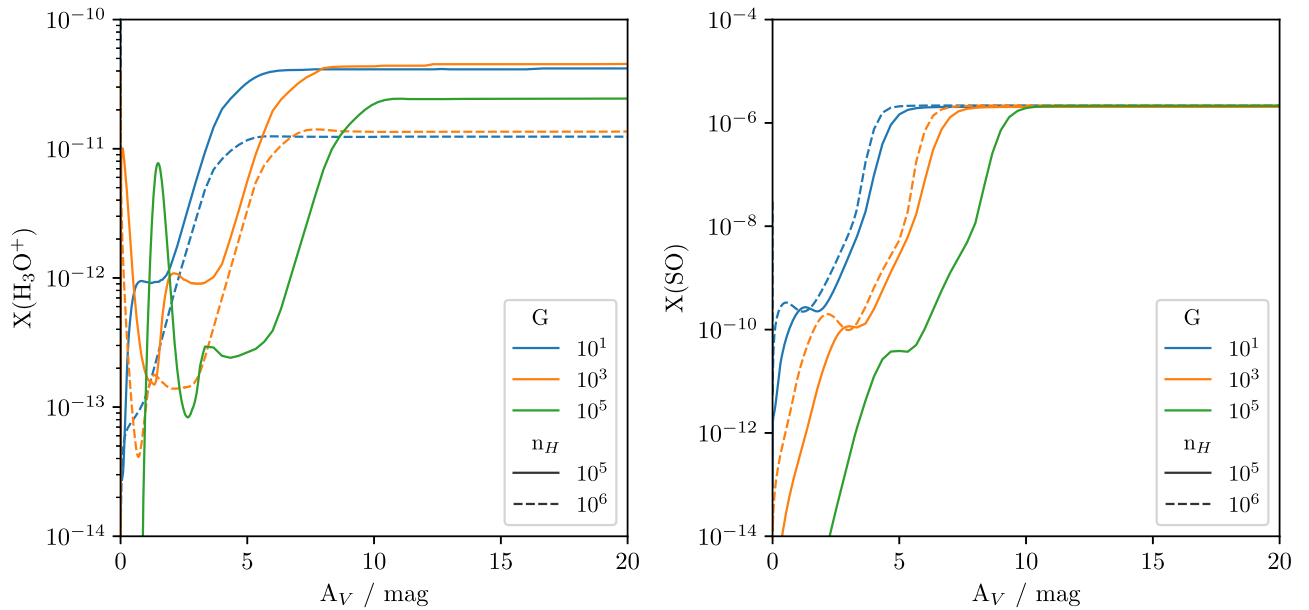_____

[25] https://github.io/UCL_PDR

Figure 4. Abundance as a function of visual extinction for H_3O^+ and SO from UCL_PDR models. The majority of these species come from within the high-A_V parts of the cloud. This is particularly true for SO, which is as much as eight orders of magnitude higher in abundance once the A_V is sufficiently high to reduce photoprocesses to zero than it is at the cloud edge.

appropriate. This is a 1D model that solves the equilibrium temperature and abundances for a semi-infinite slab of gas. Figure 4 demonstrates that for a broad range of conditions that are reasonable for the GMCs under study, the vast majority of the H_3O^+ and SO columns in these photon-dominated region (PDR) models arise from deeper within the model cloud. Thus, any H_3O^+ and SO emission from these objects should primarily trace the higher column density regions where the visual extinction is greater than 5 mag.

Finally, the possibility that shocks throughout the gas affect the ratio of H_3O^+ and SO can also be addressed through preliminary modeling. To evaluate this scenario, we generated a range of shock models using the C-shock parameterization of Jiménez-Serra et al. (2008), which includes sputtering of the ice mantles. We consider shock velocities between 5 and 40 km s^{-1} through gas with a preshock density of 1×10^5 and 1×10^6 cm^{-3}. We find that while the shock passage does tend to enhance the abundances of both species, the ratio of the two species is relatively constant at H_3O^+/SO $\sim 1 \times 10^{-4}$ in shocked gas. Thus, it will be important to test whether the abundance ratios we obtain are close to this value, but otherwise, we can assume the ratio is not dominated by shocks.

In summary, our preliminary modeling shows that the ratio of H_3O^+ and SO is strongly dependent on the ionization rate of the gas and comparatively weakly dependent on the temperature. Furthermore, the SO almost entirely arises from the inner regions of clouds with high visual extinction, and the H_3O^+ abundance is also higher in these regions than close to the cloud edge so ignoring the UV processes is justified. It is likely there are shocks present in the region under study, but they tend to produce a constant H_3O^+ to SO ratio. If the chemistry of these species is shock dominated, this can be checked a posteriori by evaluating the H_3O^+ to SO ratio found by the inference.

3.3. Parameter Inference

With the model described in Section 3.1, we can use Bayesian inference to find the probability distribution of the

values of the model parameters given the data that we observed (Section 2). From Bayes' theorem, we know this probability distribution is given by

$$p(\theta|d) = \frac{\mathcal{L}(d|\theta)p(\theta)}{p(d)}, \tag{3}$$

where θ represents the parameters and d the data. The likelihood ($\mathcal{L}(d|\theta)$) is easy to formulate as our data have normally distributed uncertainties, which allow us to use the standard Gaussian likelihood,

$$\mathcal{L}(d|\theta) = \exp\left(-\frac{1}{2}\sum_i \frac{(d_i - M_i)^2}{\sigma_i^2}\right), \tag{4}$$

where d_i is the measured intensity of one transition, σ_i is the uncertainty of that measurement, and M_i is the model spectral line intensity for a given model parameter θ.

The evidence ($p(d)$) is constant for all θ for a given model, and so we ignore it in this work. To obtain the final probability distribution $p(\theta|d)$, the probability distribution obtained from the numerator of Equation (3) is simply normalized.

Finally, a prior distribution $p(\theta)$ must be chosen. The large amount of previous work on NGC 253 provides a fantastic opportunity to set informed priors on the density (Leroy et al. 2018), column density (Mangum et al. 2019), and CRIR (Harada et al. 2021; Holdship et al. 2021). Despite this, we chose in the first instance to use uninformative priors that are uniform within limits based on those works. Finding that we adequately constrained our parameters with these uninformative priors and the data at hand, we did not progress to using informed priors. The ranges of the uniform priors are given in Table 2.

A Bayesian inference approach gives us a simple way to deal with several unknown parameters. In Table 2 we list the parameters of interest (n_H, T_{kin}, N_{H2}, ζ) as well as several nuisance parameters (ΔV, S, Z, o/p), which are unknown parameters that are not of interest to our work but may affect

Table 2
Prior Distributions Used for Each Parameter[a]

Parameter	Name	Prior Type	Range
n_H	Gas density	log-uniform	1×10^4–1×10^7 cm^{-3}
T_{kin}	Gas temperature	uniform	50–300 K
N_{H2}	H$_2$ column density	log-uniform	3×10^{22}–1×10^{25} cm^{-2}
ζ	CRIR	log-uniform	1×10^3–1×10^7 ζ_0
ΔV	Line width	uniform	50–150 km s^{-1}
S	S abundance	log-uniform	0.01–1 S$_\odot$
Z	Metallicity	uniform	0.5–3 Z$_\odot$
o/p	H$_3$O$^+$ ortho:para ratio	uniform	1–2

Note.
[a] S $\equiv$ elemental sulfur abundance at $Z = 1$ with $S_\odot$ its solar value.

our model fits. For example, it is well known that in Galactic environments, as little as 1% of sulfur is accounted for in dense gas (Charnley 1997). Thus, it is unclear how much sulfur will be available for gas-phase reactions in NGC 253 and so we leave the elemental abundance of sulfur at a metallicity of 1 as a free parameter (*S*). Including nuisance parameters in this way will account for the increased uncertainty in our inferred values for the parameters of interest due to our lack of knowledge.

In addition to the sulfur depletion factor, we consider that the exact metallicity (*Z*) of NGC 253 is unknown but is similar to the solar metallicity (Marble et al. 2010) and so we allow it to vary within a small range. We also require an ortho:para ratio of H$_3$O$^+$, which UCLCHEM does not provide. Given that this ratio has limiting values of 2 at temperatures below 50 K and 1 at temperatures above 100 K, we allow the ratio to vary freely in this range.

Finally, in order to obtain the probability distribution $P(\theta|d)$, the right-hand side of Equation (3) was sampled using `Ultranest` (Buchner 2021), which is a nested sampling package. Given the relatively computationally intensive nature of the forward model, the parameters utilized in UCLCHEM were limited in precision by rounding. The temperature was rounded to the nearest 1 K, and other UCLCHEM input parameters were rounded to the nearest 0.1 dex. This allowed model results to be saved and then if very similar parameters were requested by the sampler, the abundances could be read from the file rather than repeatedly running UCLCHEM for very small changes in parameter values. As a result, the posterior distribution of θ is limited in precision to the same degree.

4. Results

4.1. Model Spectral Line Intensities

`Ultranest` provides a set of samples from the posterior distribution weighted so that points appear in proportion to how likely they are. We use this to evaluate the goodness of fit of our model by generating the line fluxes using all points in this sample and then comparing them to the measured fluxes. The observed intensities with 1σ error bars are plotted in Figure 5 alongside the 16th to 83rd percentile range of the posterior sample fluxes. This range was chosen because for a Gaussian distribution, it is equivalent to the 1σ range.

Ignoring clear outliers, the majority of transitions show an overlap between the measurement uncertainties and the range of fluxes predicted by the model. Some outlying transitions are

to be expected considering that we are using a highly simplified model of a homogeneous sphere to fit complex regions with varying densities and temperatures. Points that do not overlap tend to be low-E_U SO transitions, which are underpredicted by the model. This is perhaps a similar effect to that seen in C$_2$H emission in the same GMCs (Holdship et al. 2021), where low-E_U emission was clearly excited by an additional gas component. However, because these deficiencies are small, we consider that the majority of the gas emitting these species is well characterized by our model.

The H$_3$O$^+$ transition at $E_u = 79.5$ K (1_1–2_1 near 307 GHz) is also often underfit. However, this is the transition that suffers from a large degree of overlap with a much stronger CH$_3$OH line as shown in Figure 2. It is possible that the overlap correction factors are too large, and we are assigning CH$_3$OH flux to the H$_3$O$^+$ line. However, the H$_3$O$^+$ transition at $E_u = 129.8$ K (3_2–2_2 near 365 GHz) is also much stronger than our models predict. No potential interloper is strong enough to explain the additional flux, but it is possible nonthermal excitation effects are contributing to the excitation of this transition. Under certain conditions, this transition can be infrared pumped (Phillips et al. 1992; Martín et al. 2021), which would explain the additional flux.

We checked that these outliers do not bias our results by fitting the GMCs excluding the 307 and 365 GHz transitions. The H3Op abundance in these models is then constrained by just the 396 GHz transition, which is not expected to be radiatively pumped (Phillips et al. 1992). We find that we obtain similar results, indicating these outliers are not strongly biasing our fit and it is primarily the fit to SO that is driving our results.

It is possible that the chemistry creates a complicating factor that prevents us from finding adequate column densities to fit the data or to simultaneously fit both species. We rule this out by fitting the data with RADEX only, treating the SO and H$_3$O$^+$ column densities as free parameters alongside the gas temperature and density. We find the same best-fit fluxes are obtained, indicating that no simple RADEX model can fit these data, and it is not the case that we simply cannot obtain the required abundances in our chemical model.

Overall, while a better radiative transfer model, or perhaps simply a multiple-gas-component fit to the data, would likely give better results, we consider that our simple model fits are sufficient. Moreover, as discussed in Section 4.3, the inference of the physical parameters allows us to validate our results using previous measurements from each GMC modeled.

4.2. Posterior Distributions

The specific values of each posterior distribution differ from GMC to GMC but the general trends are similar. We discuss here the corner plot for GMC 4 shown in Figure 6 and include the corner plots for the other GMCs modeled in Appendix B for completeness.

From the 1D marginalized posterior distributions, it is clear that we constrain three of our four parameters of interest. The gas density, the H$_2$ column density, and the CRIR are well constrained while the temperature is not. Each of the three constrained parameters has a strong peak, indicating a most likely value though the H$_2$ column density peak becomes flat below a certain limit. This is due to the fact that below a certain value, all column densities produce intensities well below the
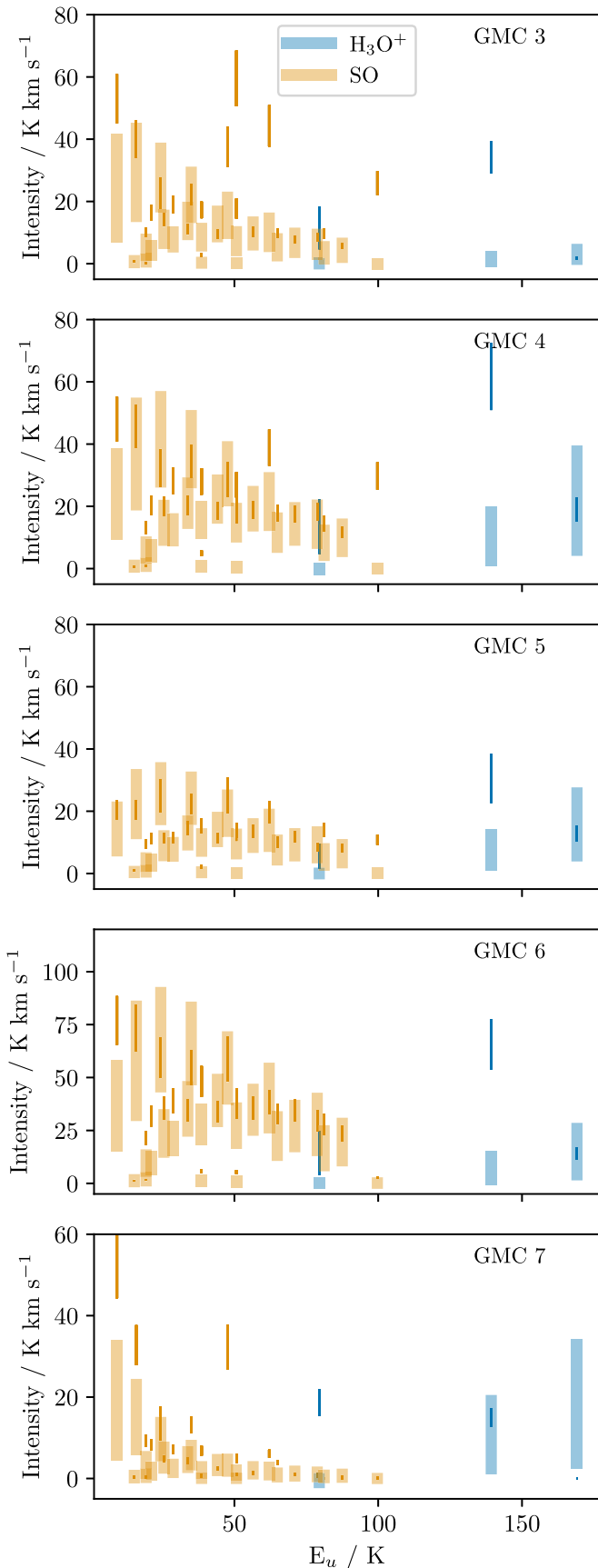
Figure 5. Measured line intensities for the GMCs plotted as error bars which cover the 1σ uncertainty range. Shaded bars show the 16th to 83rd percentiles of fluxes predicted by our model when sampling from the posterior distribution.

rms noise in our measurements and thus give identically poor fits.

The 2D joint posteriors show some interesting degeneracies. In particular, the gas density and CRIR show a log–log relationship which arises from a degeneracy in our chemical model. In UCLCHEM, the abundance can remain unchanged for increasing CRIR if the density also increases. However, because density is also a parameter of RADEX, it is constrained by radiative transfer considerations. Thus, the range of acceptable densities is greatly limited, allowing us to determine ζ despite the chemical degeneracy. Thus, without an accurate measurement of the density, we would not be able to estimate the CRIR.

Finally, there are the four nuisance parameters we included in our inference. The elemental sulfur abundance is constrained but the peak indicates that, whatever the metallicity, the elemental sulfur abundance should have a similar ratio to the other elements as found in the Sun. This means the sulfur cannot be heavily depleted onto the grains in these regions. The other nuisance parameters are unconstrained; the marginalized posteriors are very similar to the priors. This is the expected result for the line width in the case of optically thin lines. While constraining the metallicity or ortho:para ratio of H_3O^+ would have been useful, the nuisance parameters were largely included to account for their effect on the uncertainty of the CRIR, and this is achieved regardless of the fact they are unconstrained.

4.3. The GMC Properties

In this section, we present the likely values of the three parameters of interest, which we have been able to constrain. Namely, the gas density, the H_2 column density, and the CRIR. We present the most likely value of each parameter in each region as well as a most likely interval that contains 67% of the probability density, similar to a 1σ uncertainty. These are given in Table 3.

The goal of this study is ultimately to infer the CRIR in the GMCs of NGC 253. It is therefore promising that we have constrained the CRIR in every case. Each of the five GMCs has a CRIR of $\zeta \sim 1 \times 10^4\, \zeta_0$. GMC 3 has a most likely value that is a factor of 2–3 lower than the other GMCs and a significant portion of the probability density is at low values. However, it is consistent with the lower end of the range of likely values for the other GMCs and so the difference cannot be said to be significant.

The column densities we obtain are typically an order of magnitude lower than those obtained from measurements of the dust (Mangum et al. 2019). However, they are consistent with the H_2 column densities derived from observations of $C^{18}O$ (Harada et al. 2021). This agreement is important as RADEX relies on species column densities. Thus, the underlying abundances must be accurate if a good fit is achieved with a reasonable H_2 column density. This in turn gives us confidence in our inferred CRIR as we know the SO and H_3O^+ abundances are largely set by this parameter.

The gas densities are consistent with previous measurements. The range of likely density values for each region overlaps very well with those derived from the ALCHEMI observations of C_2H (Holdship et al. 2021). They also fall well within the range of 1×10^5–$1 \times 10^6\ \mathrm{cm}^{-3}$ found in other ALCHEMI work (Harada et al. 2021) and elsewhere (Leroy et al. 2018). Given
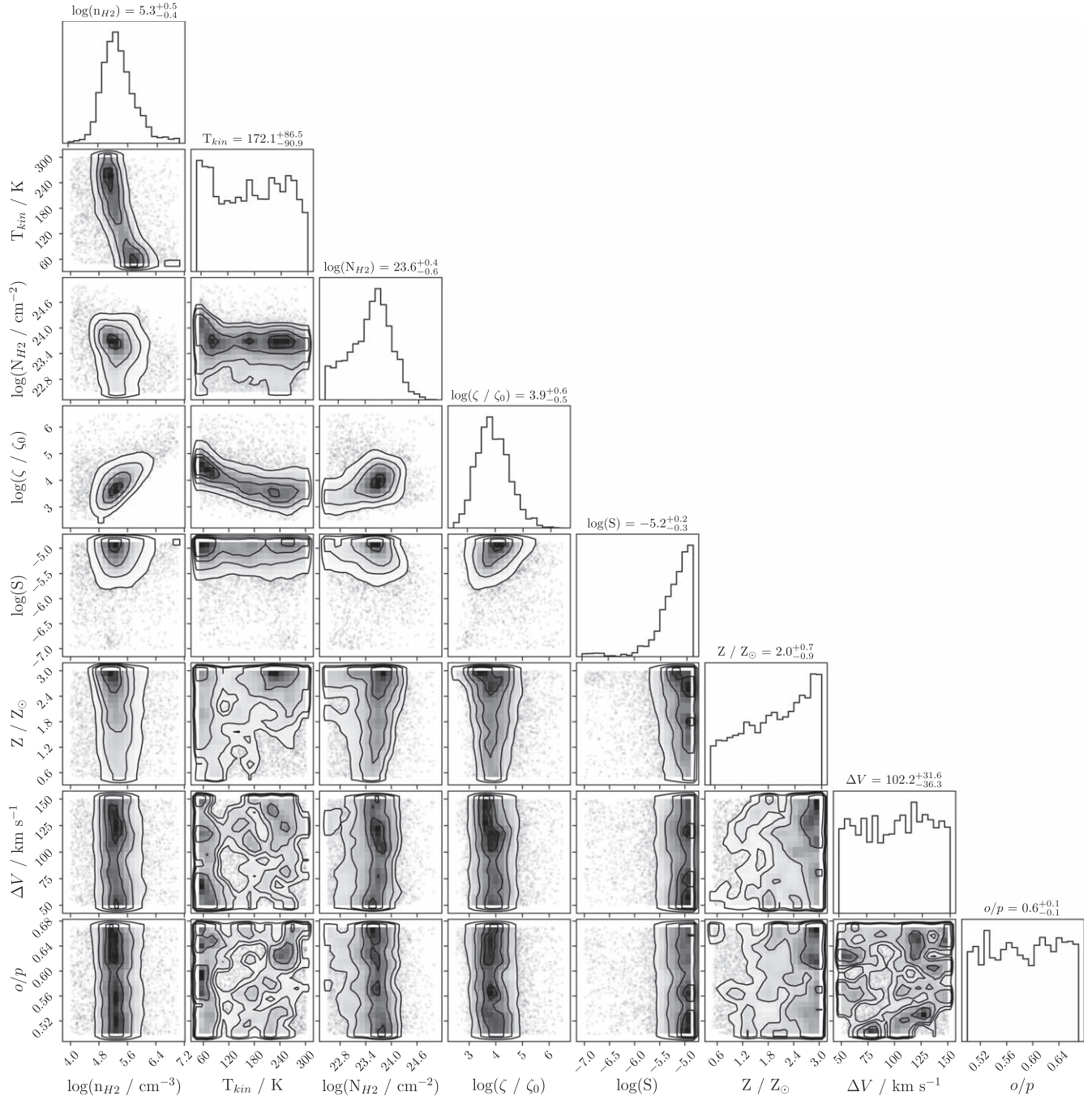
Figure 6. Corner plot showing the marginalized posterior probability distribution of every parameter and the joint distributions of all parameter pairs for GMC 4. Note the ortho:para ratio of H_3O^+ is given as the fraction of the H_3O^+ in ortho form.

Table 3
Most Likely Values of Each Well-constrained Parameter with Ranges Containing 67% of the Probability Density

GMC	$n_{H2}/1 \times 10^5$ cm^{-3}	n_{H2} Range	$N_{H2}/1 \times 10^{23}$ cm^{-2}	N_{H2} Range	$\zeta/1 \times 10^4$ ζ_0[a]	ζ Range
3	1.3	0.4–4.9	0.8	0.4–2.1	0.2	0.1–1.2
4	2.0	0.9–5.9	3.7	1.0–9.3	0.8	0.2–3.2
5	2.2	1.0–7.2	3.0	1.1–6.5	1.1	0.3–4.5
6	2.6	1.1–9.8	2.5	0.7–7.5	0.5	0.2–2.6
7	0.3	0.1–1.2	5.3	1.1–21.7	0.8	0.2–5.9

Note.
[a] $\zeta_0 = 1.36 \times 10^{-17}$ s^{-1}.
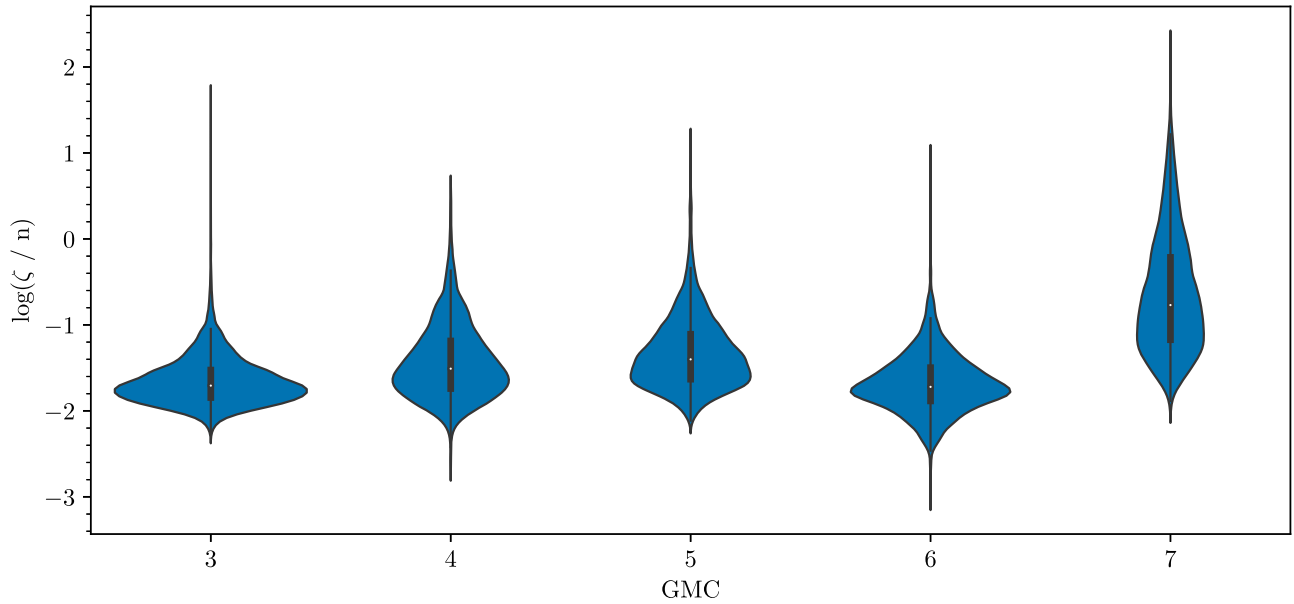
Figure 7. Violin plots showing the posterior probability distribution of ζ/n in each GMC. The width of the blue area shows the relative probability of a ζ/n value and the internal box plot marks the quartiles.

how strongly correlated ζ is with this parameter, it is key that these values are accurate. The chemical degeneracy is such that if the density were a factor of 10 lower, our inferred ζ would also be a factor of 10 smaller. Nevertheless, the good agreement with previously derived values of the gas number density from the literature should give confidence in our derived CRIR.

However, we can also combine the density and CRIR to obtain a posterior distribution on the value of ζ/n. In Figure 7, we show these distributions as violin plots. We actually constrain this value very well, indicating that a large part of the uncertainty we report on the CRIR is due to the degeneracy with density. Future use of SO and H_3O^+ as probes of the CRIR could benefit from additional data to constrain the density or stronger priors based on previous observations.

5. Discussion

5.1. The ALCHEMI View of the CRIR in NGC 253

We obtain a large CRIR that is nevertheless consistent with previous measurements. In previous ALCHEMI studies, Harada et al. (2021) found that the CRIR must be larger than $1 \times 10^3 \; \zeta_0$ across the GMCs in the CMZ of NGC 253 for chemical models to adequately explain the measured HCO^+ and HOC^+ emission. Holdship et al. (2021) also find that a CRIR of $\zeta = 1 \times 10^3 – 1 \times 10^6 \; \zeta_0$ is required to explain high column densities of C_2H. With H_3O^+ and SO, we are now able to constrain the CRIR to within an order of magnitude for the first time, with all GMCs having a CRIR $\sim 1 \times 10^4 \; \zeta_0$ or $1 \times 10^{-13} \; s^{-1}$.

It is useful to consider whether a consistent picture of the CRIR in NGC 253 is emerging from these studies. We therefore validate our inferred parameter distributions using previously reported abundances. To achieve this, we used the posterior samples provided by `Ultranest` to run UCLCHEM and probability distributions on the abundances of HCO^+, HOC^+, and C_2H according to our parameter distributions. One could include the line intensities of these species in the parameter inference but validating in this way allows us to

effectively check our fits on held-out data and evaluate the combination of H_3O^+ and SO as a probe of the CRIR.

In analogy to a 1σ interval, we define a likely range of model abundances of HCO^+, HOC^+, and C_2H by taking the 16th to 83rd percentile range of their respective distributions. We then compare these ranges to the observed abundances of those species as shown in Figure 8. In almost every case, the model and observed abundances overlap. The only exception is the C_2H abundance in GMC 4 but, statistically, one would not expect the 1σ interval of every measurement to overlap with its true value so a small difference between the model and one measurement is not surprising. The overall agreement between the model and observations indicates that we have found a consistent picture of cosmic-ray-driven chemistry in the GMCs of NGC 253.

As a further check, we also consider the abundance of H_2, CO, and e^- and include them in Figure 8. This allows us to check how strongly ionized the gas is. We find almost all H nuclei are in the form of H_2 indicating that the gas is still highly molecular under these conditions. Furthermore, for CO, we find that the CO abundance is similar to the elemental C abundance. This is important because Harada et al. (2021) reported a lower limit on the CRIR but limited it from above by the observation that a sufficiently high CRIR will dissociate CO, while observations of these regions indicate CO is abundant.

5.2. Alternatives to a High CRIR

Holdship et al. (2021) found that either a high CRIR or a scenario where the GMCs were sufficiently clumpy to allow PDR chemistry over a large column density could reproduce the observed C_2H abundance. Similarly, Harada et al. (2021) found either PDR or cosmic-ray-dominated chemistry could reproduce observed abundances of HOC^+ and HCO^+. This ambiguity is somewhat resolved by the current study, as our H_3O^+ and SO model fits greatly favor the high-CRIR scenario, largely due to the fact that H_3O^+ is destroyed by UV but enhanced by cosmic rays.
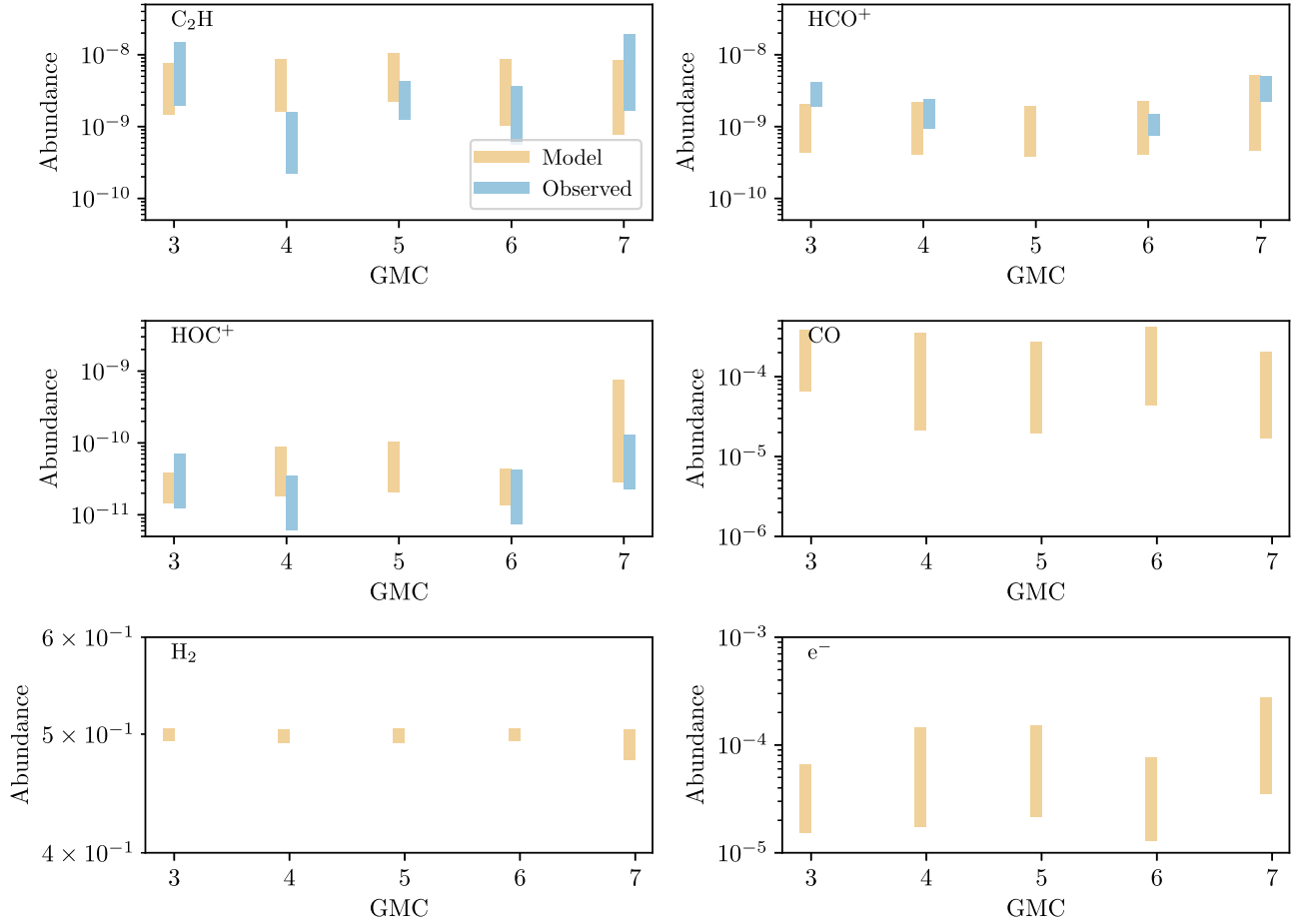
Figure 8. Abundance relative to total H nuclei of a selection of species for each region. The model range is the range of abundances obtained when sampling from the most likely portion of our parameter space using the constraints from this work. We also show observed ranges for some species which are the 1σ ranges from Holdship et al. (2021) (C_2H) and Harada et al. (2021) (HCO^+ and HOC^+). The CO, H_2, and e^- abundances are shown to demonstrate that despite the high CRIR, the gas is largely molecular.

In Section 3.2, we showed that the SO and H_3O^+ abundances are very low in PDR regions. However, when we use the posterior samples to generate model abundances for the likely parameter range, we find H_3O^+ abundances between 1×10^{-10} and 1×10^{-9}, which are too high for a PDR. Given that we have a consistent picture of CR-driven chemistry, which reproduces the abundances of C_2H, H_3O^+, SO, HOC^+, and HCO^+, a UV-dominant scenario that works for some species but not others is disfavoured.

An alternative explanation for the high C_2H abundance was the presence of ubiquitous shocks in the GMCs. In Section 3.2, we found that in shock models, the H_3O^+:SO abundance ratio was approximately 1×10^{-4} across a wide range of physical parameters. Therefore, if our inferred ratio is much different from this, it is unlikely shocks dominate the chemistry of H_3O^+ and SO. Using our posterior samples, we find that the ratio of these species' abundances varies between 0.2 and 22.9 across all regions when we consider the most likely parameter ranges given in Table 3. Because our inferred abundance ratio is always at least three orders of magnitude larger than would be found in a shock, it seems unlikely that it is in fact shock chemistry controlling the abundance of these species.

One final possibility that has not yet been discussed in this work is that of X-ray-driven chemistry. Due to their similar ionizing effect and weak attenuation with column density, X-rays can have very similar effects to cosmic rays on the

chemistry of a gas (Viti et al. 2014). Therefore, it is possible some or all of the chemistry ascribed to cosmic rays in this work is due to X-rays.

While no X-ray flux was included in the PDR models discussed in Section 3.2, UCL_PDR does treat X-rays if a flux is provided. We therefore run a model of GMC 5 using our best-fit gas density and an estimate of the largest X-ray flux that can be motivated from observations of X-ray sources around the GMCs. Lehmer et al. (2013) observed an X-ray source that they call Source B to be the brightest in NGC 253 with a luminosity of $\sim 1 \times 10^{39}$ erg. It is also very close to GMC 5, at a distance of ~ 20 pc. Combining these values, we obtain a flux of 0.05 erg cm^{-2} s^{-1}. By modeling a cloud that is subjected to this flux, we can observe the maximum effect of X-rays on our GMC chemistry.

We plot the results in Figure 9. We find that increasing the X-ray flux increases the H_3O^+ abundance and decreases the SO abundance in a similar manner to cosmic rays. However, the effect of an X-ray flux of this magnitude is not sufficient to bring the model abundances in line with observations. One could argue the H_3O^+ abundance is reasonable given the uncertainties in chemical models but the SO abundance is two orders of magnitude higher than that found from our RADEX fits. Because rectifying this with an X-ray dominated region (XDR) model would require an input X-ray flux that is orders of magnitude higher than could be expected from any observed
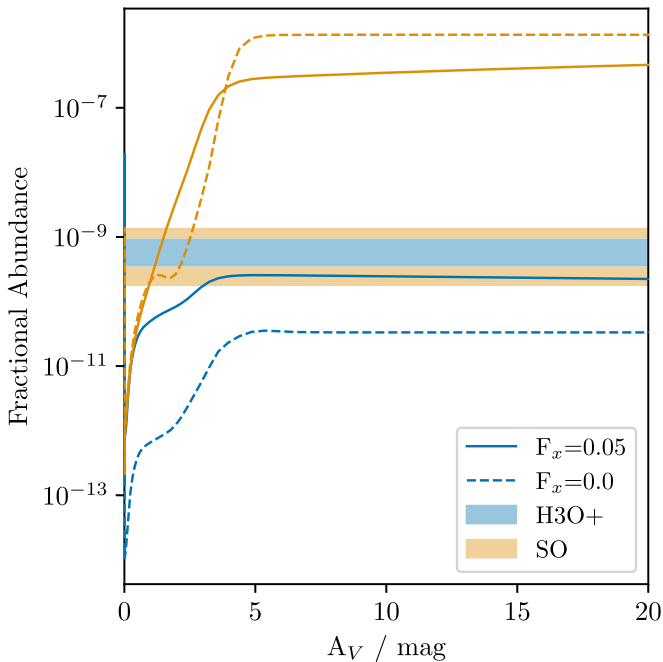
Figure 9. Lines show the modeled fractional abundance of SO and H_3O^+ as a function of visual extinction under an external X-ray flux of 0.05 erg cm^{-2} s^{-1} and under no X-ray flux. The shaded regions show the measured 67% most likely range of fractional abundances.

X-ray source, we conclude that cosmic rays must be driving most SO destruction.

6. Conclusions

Previous work has shown the CRIR in the CMZ of NGC 253 is large but has failed to constrain it to within an order of magnitude. Therefore, in this work emission from SO and H_3O^+ toward several positions in the CMZ of NGC 253 was analyzed due to the fact that their abundances are strongly tied to the CRIR.

We find that we can constrain the CRIR in these regions and that in every location it is $\sim 1 \times 10^{-13}$ s^{-1} ($1 \times 10^4 \tilde{\zeta}_0$), and is extremely unlikely to fall outside the range 1×10^{-14} to 1×10^{-12} s^{-1}. We validate this result by using our inferred parameter values to model the abundances of previously detected species that have been used as probes of the CRIR and find that we reproduce the observed abundances.

Previous ALCHEMI studies have been unable to rule out alternative processes that could explain the observed abundances of their CRIR probes. However, our inferred chemical abundances strongly disfavor shock-dominated chemistry and the high H_3O^+ abundance found in the GMCs of NGC 253

disfavors PDR chemistry. Further, the low SO abundance is unattainable with purely X-ray-driven chemistry. Because all of the CRIR tracers presented by ALCHEMI can be consistently modeled through cosmic-ray-dominated chemistry, we now consider this to be the most likely scenario.

We find no evidence for variation in the CRIR between the GMCs we have modeled. While GMCs 3 and 7 have the lowest most likely CRIR values, the uncertainties in those values are sufficiently large that they overlap considerably with the CRIR values derived for other GMCs. Given that the model already fails to capture the complexity of the data, it is likely a more accurate model is required rather than more data in order to better constrain the CRIR in each GMC.

Appendix A
The ALCHEMI H_3O^+ and SO Data

In this section, we present the data analyzed in this work. In Figures 10 and 11, we show additional moment 0 maps of NGC 253's CMZ. We also provide an example of the data included in the supplementary data table. Table 4 shows the transitions and measured line intensities detected in GMC 4, the equivalent values for the other GMCs are available.
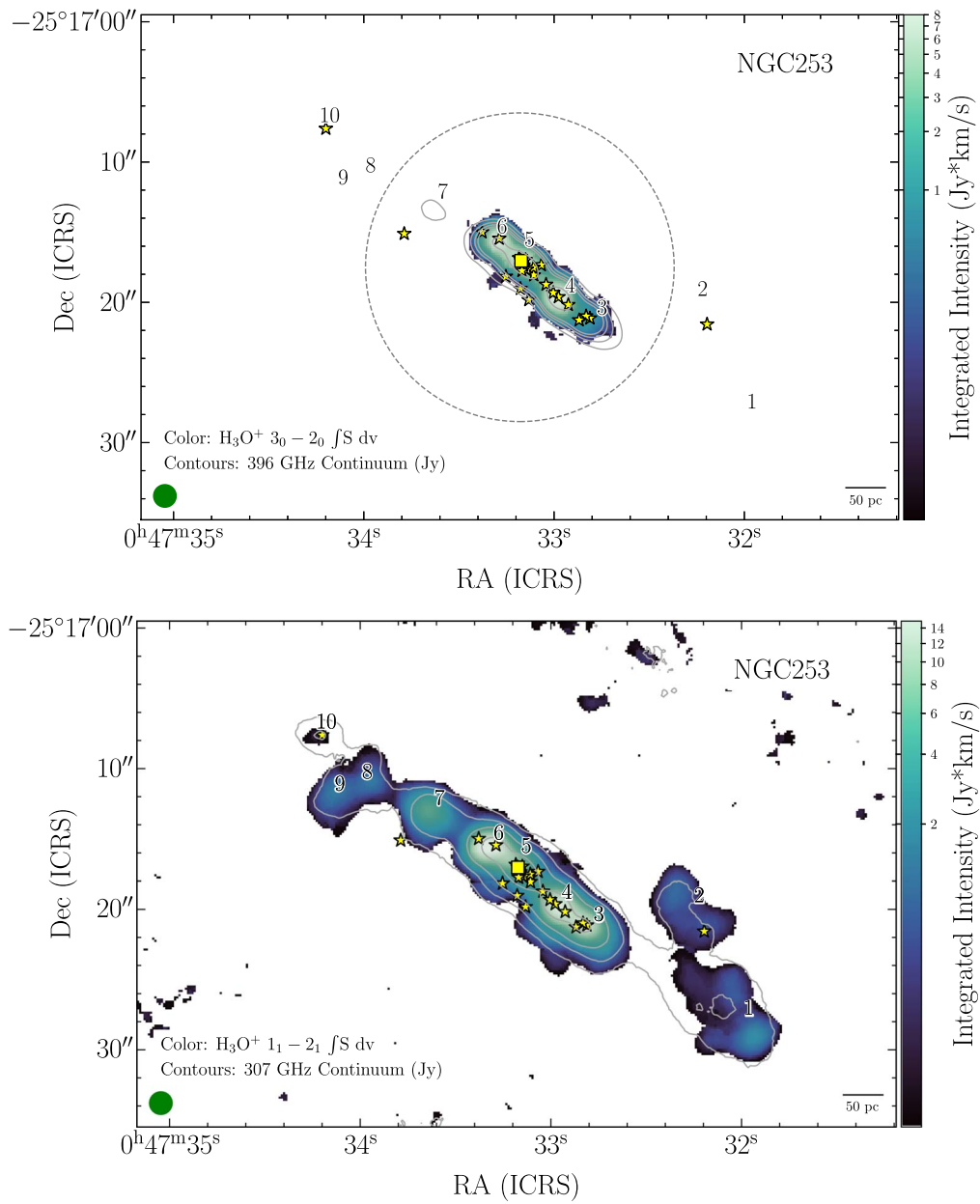
Figure 10. Additional H_3O^+ integrated intensity (moment 0) images toward NGC 253. Markings, intensity scaling, and contours in each panel same as in Figure 1. The continuum rms values for the transitions shown are 10.0 and 1.0 mJy beam^{-1}, respectively. Note that the field of view for the $H_3O^+ 3_0 - 2_0$ transition is 22'' centered at $\alpha = 00^h47^m33.134^s$, $\delta = -25°17'19.68''$ (shown as a grey dashed circle; ICRS; see Section 2.2).
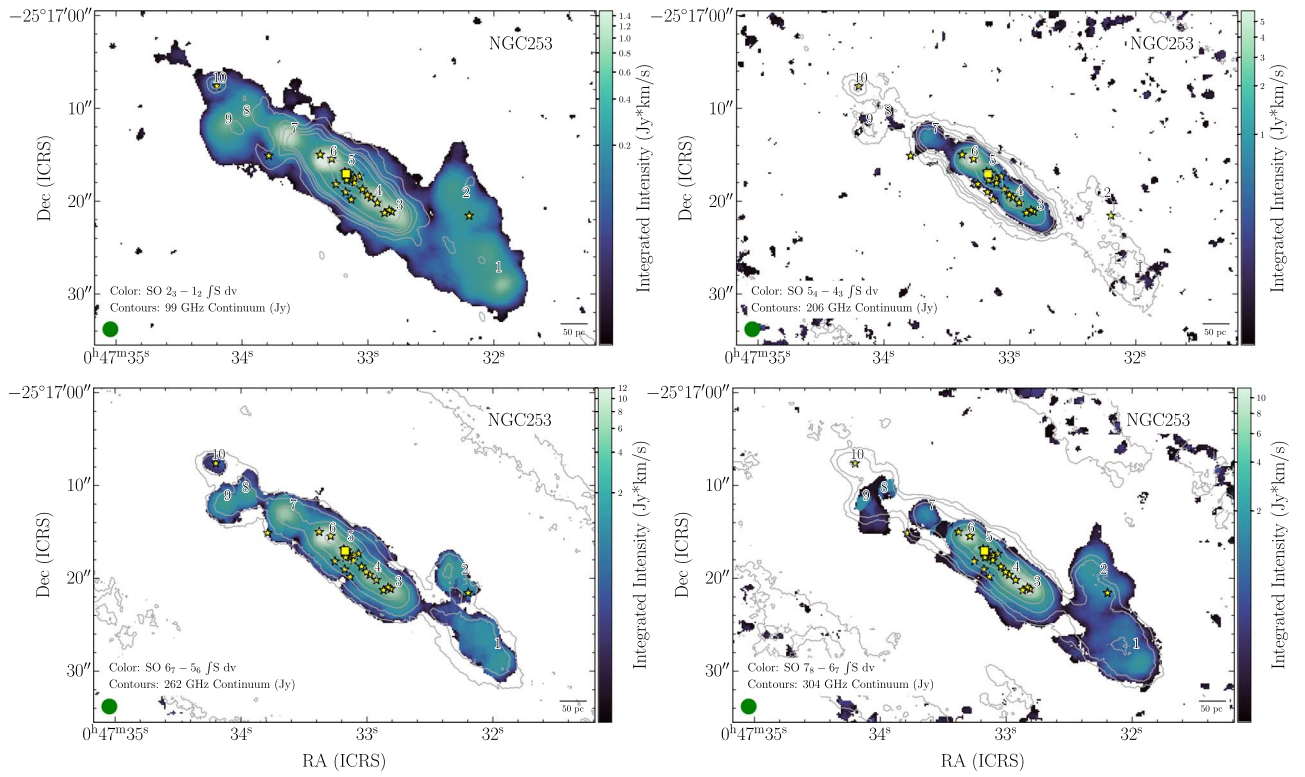
Figure 11. Additional SO integrated intensity (moment 0) images toward NGC 253. Markings, intensity scaling, and contours in each panel same as in Figure 1. The continuum rms values for the transitions shown are 0.17, 0.17, 0.33, 0.33, and 0.33 mJy beam^{-1}, respectively.

Table 4
Detected Transitions, Their Properties, and Measured Intensities for GMC 4

Region	Species	Transition	Frequency (GHz)	E_U (K)	R.A.	Decl.	Corrected Integrated Intensity (K km s^{-1})	Integrated Intensity Uncertainty (K km s^{-1})	Interloper Correction
4	H3Op	1.1.1–2.1.0	307.192410	79.5	11.8874	−25.28888	13.509450	8.817727	0.23
4	H3Op	3.2.0–2.2.1	364.797430	139.3	11.8874	−25.28888	61.744377	10.782524	0.86
4	H3Op	3.0.1–2.0.0	396.272410	169.1	11.8874	−25.28888	18.992481	3.812451	1.00
4	SO	2.3–1.2	99.299870	9.2	11.8874	−25.28888	47.964352	7.209908	1.00
4	SO	1.1–0.1	286.340152	15.2	11.8874	−25.28888	0.591833	0.354076	1.00
4	SO	3.4–2.3	138.178600	15.9	11.8874	−25.28888	45.781056	6.875517	1.00
4	SO	2.2–1.1	86.093950	19.3	11.8874	−25.28888	13.188165	2.028540	1.00
4	SO	2.2–1.2	309.502444	19.3	11.8874	−25.28888	0.973434	0.366215	1.00
4	SO	3.2–2.1	109.252220	21.1	11.8874	−25.28888	20.209262	3.069187	1.00
4	SO	4.5–3.4	178.605403	24.4	11.8874	−25.28888	32.354178	6.111951	1.00
4	SO	3.3–2.2	129.138923	25.5	11.8874	−25.28888	20.025210	3.028742	1.00
4	SO	4.3–3.2	158.971811	28.7	11.8874	−25.28888	28.146298	4.251155	1.00
4	SO	4.4–3.3	172.181403	33.8	11.8874	−25.28888	20.281011	3.075113	1.00
4	SO	5.6–4.5	219.949442	35.0	11.8874	−25.28888	34.456452	5.173552	1.00
4	SO	5.4–4.3	206.176005	38.6	11.8874	−25.28888	27.974328	4.237034	1.00
4	SO	5.4–4.4	100.029640	38.6	11.8874	−25.28888	4.935441	0.872624	1.00
4	SO	5.5–4.4	215.220653	44.1	11.8874	−25.28888	18.644894	2.810657	1.00
4	SO	6.7–5.6	261.843721	47.6	11.8874	−25.28888	28.611328	5.660309	0.76
4	SO	6.5–5.4	251.825770	50.7	11.8874	−25.28888	20.277435	5.747689	0.53
4	SO	6.5–5.5	136.634799	50.7	11.8874	−25.28888	26.897403	4.049473	1.00
4	SO	6.6–5.5	258.255826	56.5	11.8874	−25.28888	18.888161	2.867306	1.00
4	SO	7.8–6.7	304.077844	62.1	11.8874	−25.28888	38.849257	5.843079	1.00
4	SO	7.6–6.5	296.550064	64.9	11.8874	−25.28888	17.696586	2.673156	1.00
4	SO	7.7–6.6	301.286124	71.0	11.8874	−25.28888	17.585570	2.662084	1.00
4	SO	8.9–7.8	346.528481	78.8	11.8874	−25.28888	18.149714	2.795038	1.00
4	SO	8.7–7.6	340.714155	81.2	11.8874	−25.28888	14.417925	2.531354	0.87
4	SO	8.8–7.7	344.310612	87.5	11.8874	−25.28888	11.763875	1.843587	0.99
4	SO	9.8–8.8	254.573628	99.7	11.8874	−25.28888	29.755258	4.477287	1.00

(This table is available in its entirety in machine-readable form.)

Appendix B
Corner Plots

In this section, we include the corner plots for GMCs 3, 5, 6, and 7 (Figures 12–15), which are not in the main article.
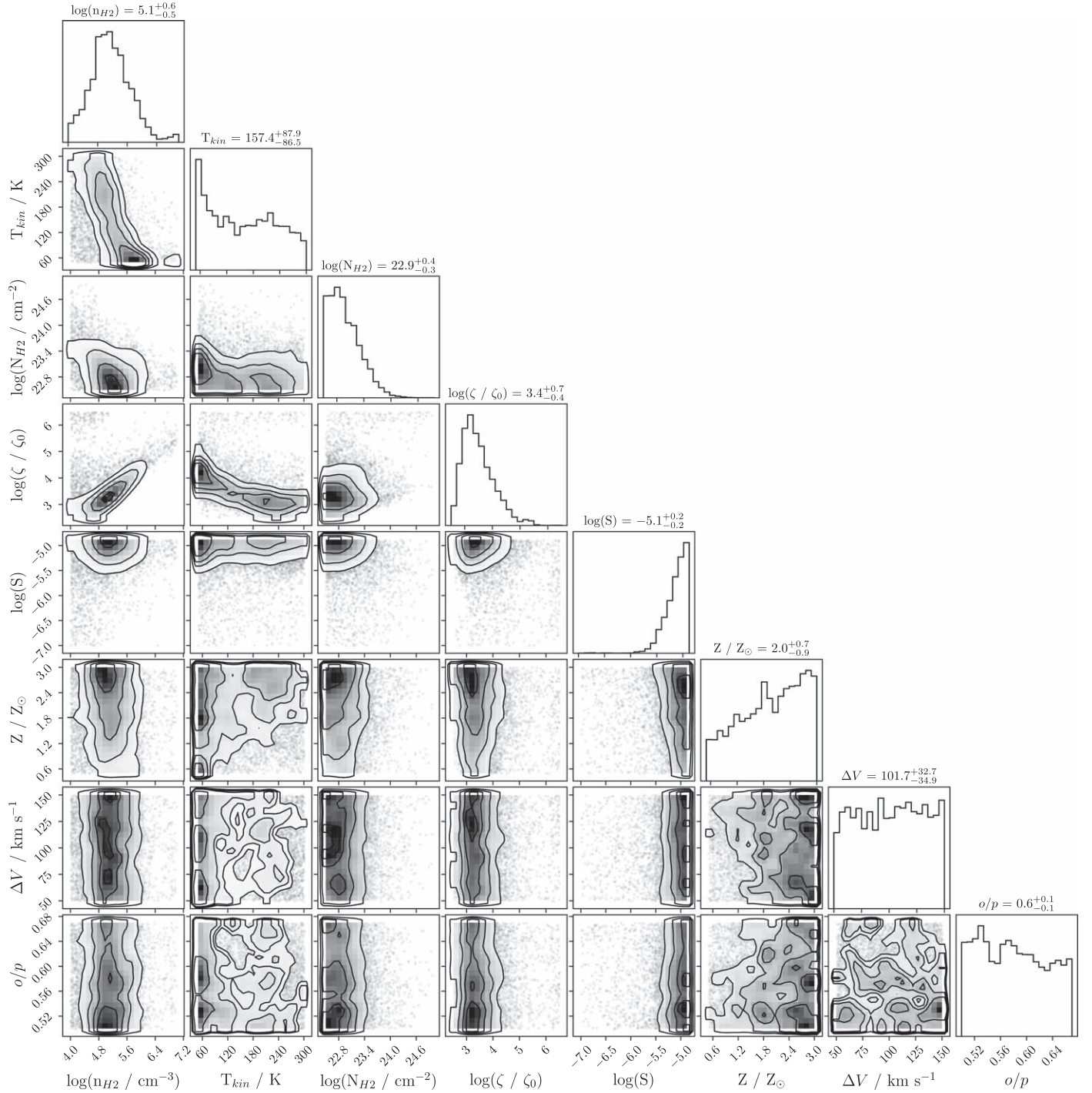

Figure 12. Corner plot showing the marginalized posterior probability distribution of every parameter and the joint distributions of all parameter pairs for GMC 3.
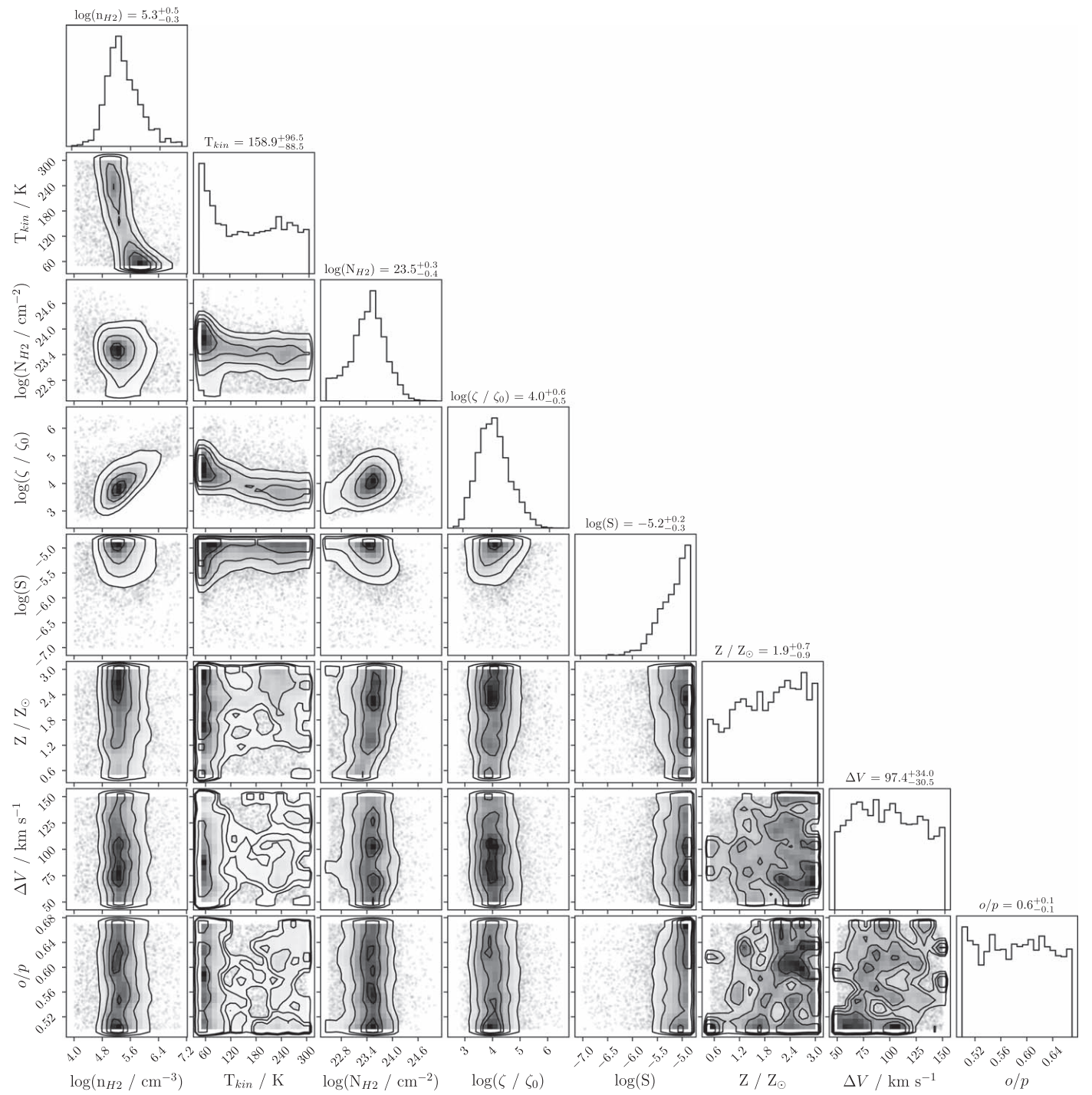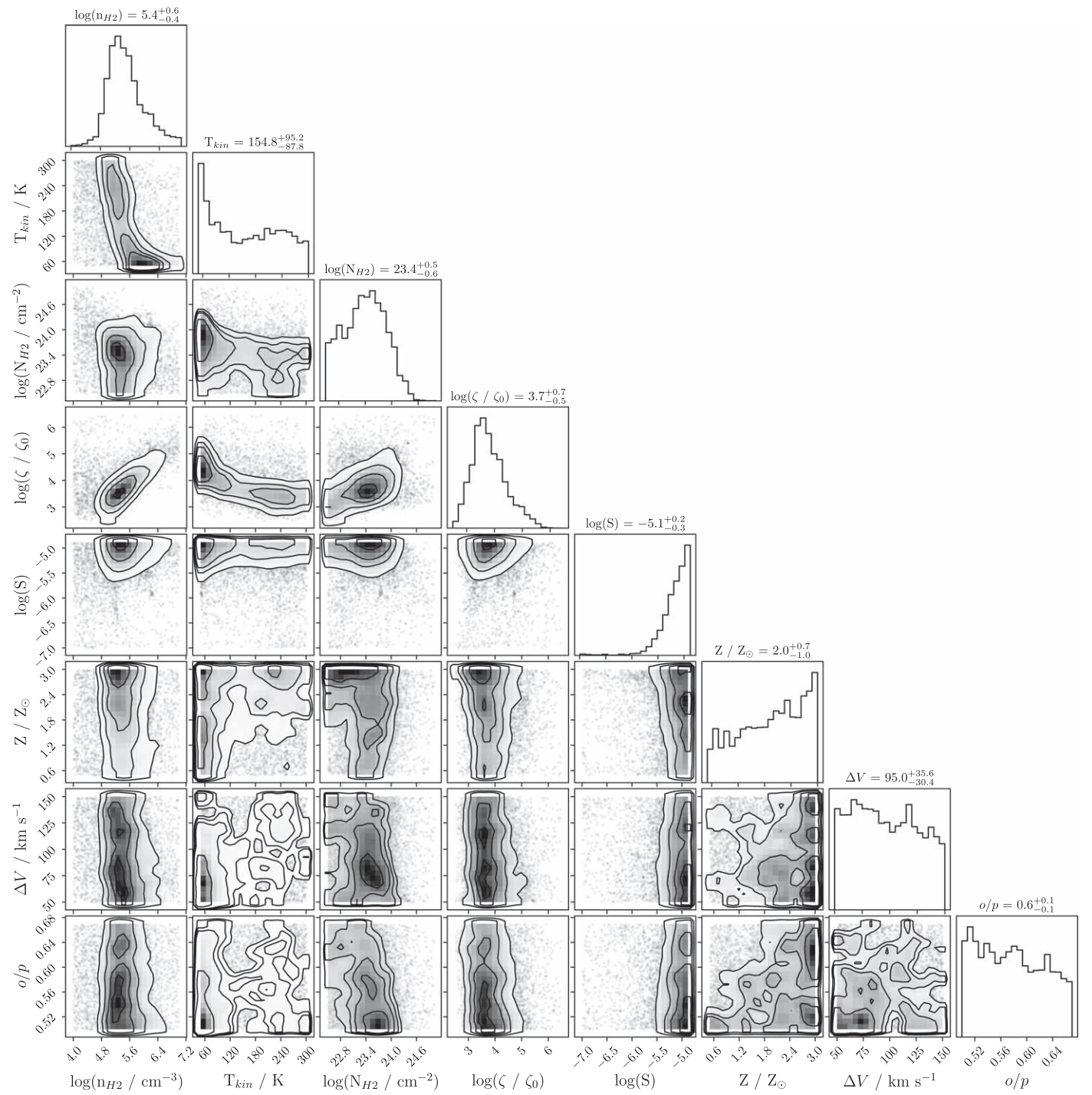
Figure 13. Similar to Figure 12 for GMC 5.

Figure 14. Similar to Figure 12 for GMC 6.

Figure 15. Similar to Figure 12 for GMC 7.
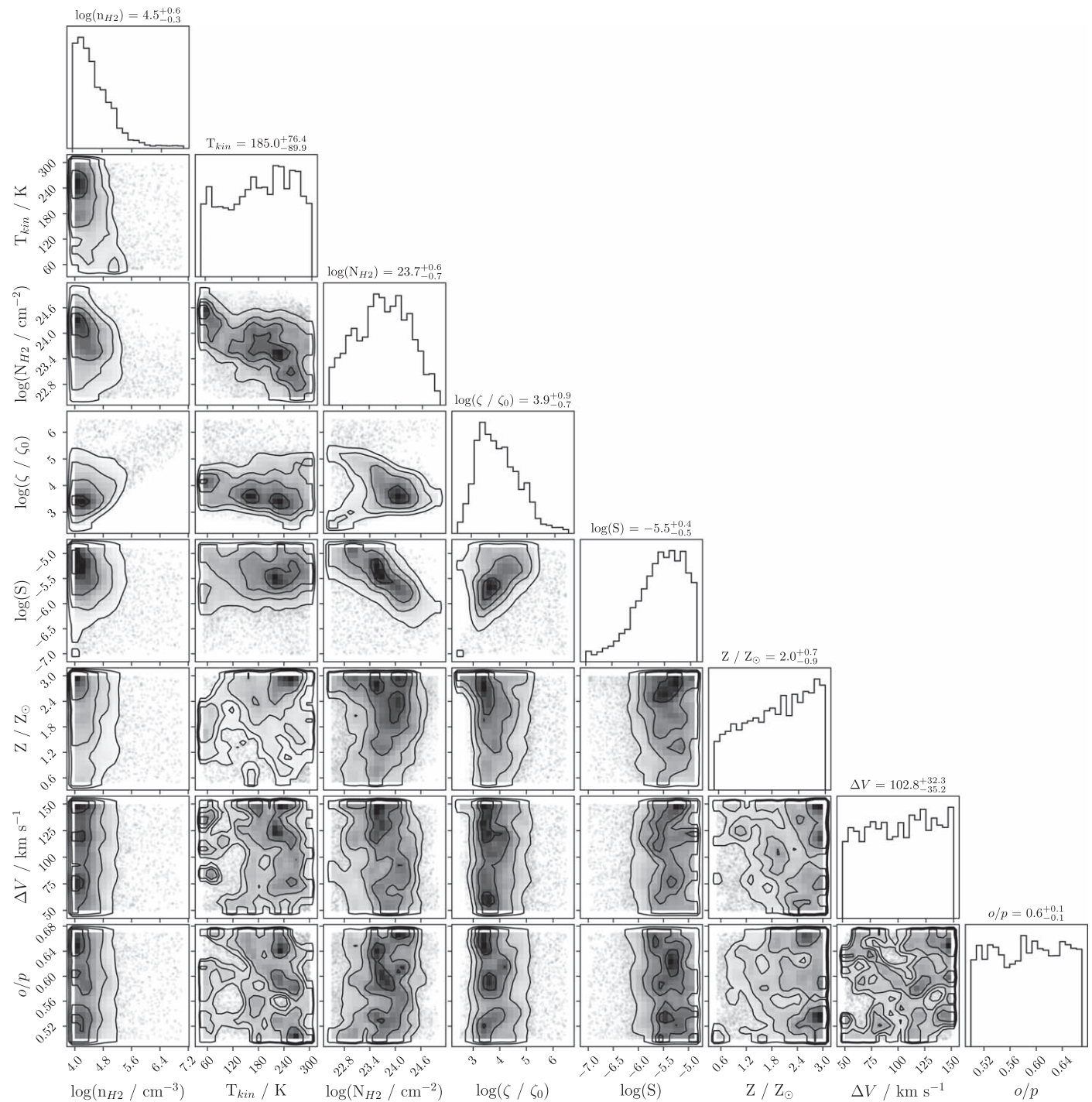
ORCID iDs

Jonathan Holdship

Jeffrey G. Mangum

Serena Viti

Erica Behrens

Nanase Harada

Sergio Martín

Kazushi Sakamoto

Sebastien Muller

Kunihiko Tanaka

Kouichiro Nakanishi

Yuki Yoshimura

Rebeca Aladro

Laura Colzi

Kimberly L. Emig

Christian Henkel

Yuri Nishimura

Víctor M. Rivilla

Paul P. van der Werf

References

Bayet, E., Williams, D. A., Hartquist, T. W., & Viti, S. 2011, MNRAS, 414, 1583

Bell, T. A., Hartquist, T., Viti, S., & Williams, D. A. 2006, A&A, 459, 805

Buchner, J. 2021, JOSS, 6, 3001

Charnley, S. B. 1997, ApJ, 481, 396

Demes, S., Lique, F., Faure, A., et al. 2021, MNRAS, 509, 1252

Gerin, M., De Luca, M., Black, J., et al. 2010, A&A, 518, L110

Goldsmith, P. F. 2001, ApJ, 557, 736

González-Alfonso, E., Fischer, J., Bruderer, S., et al. 2013, A&A, 550, A25

Harada, N., Martín, S., Mangum, J. G., et al. 2021, ApJ, 923, 24

Holdship, J., Viti, S., Jiménez-Serra, I., Makrymallis, A., & Priestley, F. 2017, AJ, 154, 38

Holdship, J., Viti, S., Martín, S., et al. 2021, A&A, 654, A55

Indriolo, N., Neufeld, D. A., Gerin, M., et al. 2015, ApJ, 800, 40

Jenkins, E. B. 2009, ApJ, 700, 1299

Jiménez-Serra, I., Caselli, P., Martín-Pintado, J., & Hartquist, T. 2008, A&A, 482, 549

Lehmer, B. D., Wik, D. R., Hornschemeier, A. E., et al. 2013, ApJ, 771, 134

Leroy, A. K., Bolatto, A. D., Ostriker, E. C., et al. 2015, ApJ, 801, 25

Leroy, A. K., Bolatto, A. D., Ostriker, E. C., et al. 2018, ApJ, 869, 126

Lique, F., Dubernet, M.-L., Spielfiedel, A., & Feautrier, N. 2006, A&A, 450, 399

Mangum, J. G., Ginsburg, A. G., Henkel, C., et al. 2019, ApJ, 871, 170

Marble, A. R., Engelbracht, C. W., Van Zee, L., et al. 2010, ApJ, 715, 506

Martín, S., Martín-Pintado, J., Blanco-Sánchez, C., et al. 2019, A&A, 631, A159

Martín, S., Mauersberger, R., Martín-Pintado, J., Henkel, C., & García-Burillo, S. 2006, ApJS, 164, 450

Martín, S., Mangum, J. G., Harada, N., et al. 2021, A&A, 656, A46

McElroy, D., Walsh, C., Markwick, A. J., et al. 2013, A&A, 550, A36

Muller, S., Müller, H. S., Black, J. H., et al. 2016, A&A, 595, A128

Padovani, M., Galli, D., & Glassgold, A. E. 2009, A&A, 501, 619

Padovani, M., Ivlev, A. V., Galli, D., & Caselli, P. 2018, A&A, 614, A111

Phillips, T. G., van Dishoeck, E. F., & Keene, J. 1992, ApJ, 399, 533

Priestley, F., Barlow, M. J., & Viti, S. 2017, MNRAS, 472, 4444

Rekola, R., Richer, M. G., McCall, M. L., et al. 2005, MNRAS, 361, 330

Sakamoto, K., Mao, R. Q., Matsushita, S., et al. 2011, ApJ, 735, 19

Schöier, F. L. L., van der Tak, F. F. S., van Dishoeck, E. F., & Black, J. H. 2005, A&A, 432, 369

Turner, J. L., Ho, P. T. P., Turner, J. L., & Ho, P. T. P. 1985, ApJL, 299, L77

Ulvestad, J. S., Antonucci, R. R. J., Ulvestad, J. S., & Antonucci, R. R. J. 1997, ApJ, 488, 621

van der Tak, F. F. S., Black, J. H. H., Schöier, F. L. L., Jansen, D. J. J., & Van Dishoeck, E. F. 2007, A&A, 468, 627

Viti, S., García-Burillo, S., Fuente, A., et al. 2014, A&A, 570, A28

Williams, D. A., & Viti, S. 2013, Observational Molecular Astronomy, Vol. 1 (Cambridge: Cambridge Univ. Press)